REPORT DOCUMENTATION PAGE

Form Approved OMB NO. 0704-0188

The public reporting burden for this collection of information is estimated to average 1 hour per response, including the time for reviewing instructions, searching existing data sources, gathering and maintaining the data needed, and completing and reviewing the collection of information. Send comments regarding this burden estimate or any other aspect of this collection of information, including suggesstions for reducing this burden, to Washington Headquarters Services, Directorate for Information Operations and Reports, 1215 Jefferson Davis Highway, Suite 1204, Arlington VA, 22202-4302. Respondents should be aware that notwithstanding any other provision of law, no person shall be subject to any oenalty for failing to comply with a collection of information if it does not display a currently valid OMB control number.
PLEASE DO NOT RETURN YOUR FORM TO THE ABOVE ADDRESS.

1. REPORT DATE (DD-MM-YYYY)	2. REPORT TYPE	3. DATES COVERED (From - To)
16-05-2010	Final Report	1-Jun-2007 - 31-May-2010

4. TITLE AND SUBTITLE	5a. CONTRACT NUMBER
Final Report on Terahertz Microscope	W911NF-07-1-0278
	5b. GRANT NUMBER
	5c. PROGRAM ELEMENT NUMBER
	611102

6. AUTHORS	5d. PROJECT NUMBER
X.-C. Zhang	5e. TASK NUMBER
	5f. WORK UNIT NUMBER

7. PERFORMING ORGANIZATION NAMES AND ADDRESSES	8. PERFORMING ORGANIZATION REPORT NUMBER
Rensselaer Polytechnic Institute Office of Sponsored Research Rensselaer Polytechnic Institute Troy, NY 12180 -	

9. SPONSORING/MONITORING AGENCY NAME(S) AND ADDRESS(ES)	10. SPONSOR/MONITOR'S ACRONYM(S)
U.S. Army Research Office P.O. Box 12211 Research Triangle Park, NC 27709-2211	ARO
	11. SPONSOR/MONITOR'S REPORT NUMBER(S)
	50519-EL.1

12. DISTRIBUTION AVAILIBILITY STATEMENT

Approved for Public Release; Distribution Unlimited

13. SUPPLEMENTARY NOTES

The views, opinions and/or findings contained in this report are those of the author(s) and should not contrued as an official Department of the Army position, policy or decision, unless so designated by other documentation.

14. ABSTRACT

The primary objective of this project is to develop and demonstrate a suitable THz-wave apparatus as a THz imaging platform with a deep sub-wavelength spatial resolution for Army application; potentially for chemical/biological (CB) detection. The spatial resolution of the new T-ray microscopic imaging platform is orders of magnitude greater than that which is available in a standard free-space T-ray imaging system, with the target of nanometer resolution. This allows us to explore the rich, spectroscopic signatures of hetero-structure, quantum dots,

15. SUBJECT TERMS

terahertz microscope, imaging, sensing, photonics

16. SECURITY CLASSIFICATION OF:			17. LIMITATION OF ABSTRACT	15. NUMBER OF PAGES	19a. NAME OF RESPONSIBLE PERSON
a. REPORT	b. ABSTRACT	c. THIS PAGE			Xi-Cheng Zhang
UU	UU	UU	UU		19b. TELEPHONE NUMBER
					518-276-3079

Report Title

Final Report on Terahertz Microscope

ABSTRACT

The primary objective of this project is to develop and demonstrate a suitable THz-wave apparatus as a THz imaging platform with a deep sub-wavelength spatial resolution for Army application; potentially for chemical/biological (CB) detection. The spatial resolution of the new T-ray microscopic imaging platform is orders of magnitude greater than that which is available in a standard free-space T-ray imaging system, with the target of nanometer resolution. This allows us to explore the rich, spectroscopic signatures of hetero-structure, quantum dots, devices and IC circuit diagnostics and molecular vibrations, rotations, and other low-energy transitions for chemical/biological sensing and imaging applications.

During the period of this research, the major activities and achievements are in three areas: THz-wave emission microscope, THz near-field microscope using taper waveguide, and THz photonic devices for THz spectroscopy system.

List of papers submitted or published that acknowledge ARO support during this reporting period. List the papers, including journal references, in the following categories:

(a) Papers published in peer-reviewed journals (N/A for none)

Y. T. Chen, P. Y. Han, and X.-C. Zhang, "Tunable broadband antireflection structures for silicon at terahertz frequency", Applied Physics Letters, 94, 041106 (2009).

Research Highlights, "terahertz trials: the Great pyramids of silicon", Nature Photonics, 3, 187, April (2009)

P. Y. Han, Y. T. Chen, and X.-C. Zhang, "Application of Silicon Micro-pyramid Structures for Anti-reflection of Terahertz Waves", IEEE J. Sel. Topic Quant. Electro., DOI 10.1109/JSTQE.2009.2031164 (2009).

J. Chen, P. Y. Han, and X.-C. Zhang, "Terahertz-field-induced second-harmonic generation in a beta barium borate crystal and its application in terahertz detection", Appl. Phys. Lett. V. 95, 011118 (2009).

P. Y. Han, W. Liu, Y.-H Xie and X.-C. Zhang, "Graphene and terahertz science", Wuli, V. 38, No. 6, p. 395-400 (2009).

Y. T. Chen, P. Y. Han, and X.-C. Zhang, "Silicon-based multi-layer anti-reflection structures for terahertz application", To be submitted to Optics Letter, (2009).

Patric Lockhart and P.S. Dutta, Pengyu Han and X.-C. Zhang, "Terahertz Emission Mechanisms in $InAs_xP1-x$," Appl. Phys. Letts., 92, 011102 (2008).

Albert Redo-Sanchez and X.-C. Zhang, "Terahertz Science and Technology Trends," Journal of Selected Topics in Quantum Electronics, 14, 260 (2008).

Number of Papers published in peer-reviewed journals: 8.00

(b) Papers published in non-peer-reviewed journals or in conference proceedings (N/A for none)

Number of Papers published in non peer-reviewed journals: 0.00

(c) Presentations

Pengyu Han, Yuting W. Chen, and X.-C. Zhang, "Application of Silicon Photonic devices as an Anti-reflection Layer for Terahertz Waves", Nanoelectronic Devices for Defense & Security Conference (2009).

Yuting W. Chen, "Application of Silicon Photonic Crystals for Anti-reflection of Terahertz Waves", IGERT Annual Meeting (2009).

X.-C. Zhang, "Recent development of THz wave science and technology," Vilnius University and Institute of Semiconductor, Vilnius, Lithuania, April 16, (2008).

X.-C. Zhang, "Recent development on THz wave science and technology," Keynote, NATO SET129 Specialist Meeting, Bucharest, Romania, May 20, 2008.

X.-C. Zhang, "Recent progress on THz sensing and imaging," Workshop on Terahertz (THz) Science & Technology, Singapore, May 29, 2008.

Albert Redo, Pierre Servais, X.-C. Zhang, "Inspection of military protective equipment with Terahertz imaging," NATO SET129 Specialist Meeting, Bucharest, Romania, May 20, 2008.

David Brigada, Brian Schulkin, and X.-C. Zhang, "Chemical Threat Detection Via Portable THz Spectroscopy," 2008 International Symposium on Spectral Sensing Research, Stevens Institute of Technology, NJ, June 24-25, 2008.

Yunqing Chen, Nick Karpowicz, Xiaofei Lu, Minfeng Wang, Masashi Yamaguchi, X.-C. Zhang, "THz Generation from Inert Gases & Chemical Vapor", 2008 International Symposium on Spectral Sensing Research, Stevens Institute of Technology, NJ, June 27, 2008.

Brian Schulkin and X.-C Zhang, "Quality Assurance of Real-Time Terahertz Wave Sensing", 2008 International Symposium on Spectral Sensing Research, Stevens Institute of Technology, NJ, June 25, 2008.

Brian Schulkin, Guangyin Zeng, X.-C. Zhang, "Performance of Real-Time Chemical Sensing with a Handheld THz Spectrometer", 2008 International Symposium on Spectral Sensing Research, Stevens Institute of Technology, NJ, June 27, 2008.

P.Y. Han, J. Chen, H.W. Zhao, B. Schulkin, Y.Q. Chen, G. Bastiaans, J. Warrender, and X.-C. Zhang, "Application of Terahertz Spectroscopy in Security, chemistry and Microscopy" Laser Applications to Chemical, Security and Environmental Analysis (LACSEA) Invited Speaker Invitation, St. Petersburg, FL, March 18, 2008.

Number of Presentations: 11.00

Non Peer-Reviewed Conference Proceeding publications (other than abstracts):

Pengyu Han, Yuting W. Chen, and X.-C. Zhang, "Application of Silicon Photonic devices as an Anti-reflection Layer for Terahertz Waves", Nanoelectronic Devices for Defense & Security Conference (2009).

Number of Non Peer-Reviewed Conference Proceeding publications (other than abstracts):   0

Peer-Reviewed Conference Proceeding publications (other than abstracts):

Pengyu Han, Yuting W. Chen, and X.-C. Zhang, "Application of Silicon Photonic devices as an Anti-reflection Layer for Terahertz Waves", Nanoelectronic Devices for Defense & Security Conference (2009).

Number of Peer-Reviewed Conference Proceeding publications (other than abstracts):   1

(d) Manuscripts

Number of Manuscripts: 0.00

Patents Submitted

Tunable Broadband Anti-Reflection Apparatus for Silicon at Terahertz Frequency

Patents Awarded

Graduate Students

NAME	PERCENT_SUPPORTED
FTE Equivalent:	
Total Number:	

Names of Post Doctorates

NAME	PERCENT_SUPPORTED
FTE Equivalent:	
Total Number:	

Names of Faculty Supported

NAME	PERCENT_SUPPORTED	National Academy Member
Zhang, Xi-Cheng	0.50	No
FTE Equivalent:	**0.50**	
Total Number:	**1**	

Names of Under Graduate students supported

NAME	PERCENT_SUPPORTED
FTE Equivalent:	
Total Number:	

Student Metrics
This section only applies to graduating undergraduates supported by this agreement in this reporting period

The number of undergraduates funded by this agreement who graduated during this period: 0.00

The number of undergraduates funded by this agreement who graduated during this period with a degree in science, mathematics, engineering, or technology fields: 0.00

The number of undergraduates funded by your agreement who graduated during this period and will continue to pursue a graduate or Ph.D. degree in science, mathematics, engineering, or technology fields: 0.00

Number of graduating undergraduates who achieved a 3.5 GPA to 4.0 (4.0 max scale): 0.00

Number of graduating undergraduates funded by a DoD funded Center of Excellence grant for Education, Research and Engineering: 0.00

The number of undergraduates funded by your agreement who graduated during this period and intend to work for the Department of Defense 0.00

The number of undergraduates funded by your agreement who graduated during this period and will receive scholarships or fellowships for further studies in science, mathematics, engineering or technology fields: 0.00

Names of Personnel receiving masters degrees

NAME
Xiaoyu Guo

Total Number: 1

Names of personnel receiving PHDs

NAME

Total Number:

Names of other research staff

NAME   PERCENT_SUPPORTED

FTE Equivalent:
Total Number:

Sub Contractors (DD882)

Inventions (DD882)

5 **Tunable Broadband Anti-Reflection Apparatus for Silicon at Terahertz Frequency**

Patent Filed in US? (5d-1)   Y

Patent Filed in Foreign Countries? (5d-2)   N

Was the assignment forwarded to the contracting officer? (5e)   N

Foreign Countries of application (5g-2):

    5a: Chen, Yuting

  5f-1a: RPI

   5f-c: 110 8th St

     Troy   NY   12180

    5a: Han, Pengyu

  5f-1a: RPI

   5f-c: 110 8th St

     Troy   NY   12180

    5a: Zhang, Xi-Cheng

  5f-1a: RPI

   5f-c: 110 8th St

     Troy   NY   12180

Final Report on Terahertz Microscope

Final Report Requirement for Proposal Number: 50519-EL, Agreement Number: W911NF-07-1-0278

Prepared by Professor X.-C. Zhang

Center for Terahertz Research, Rensselaer Polytechnic Institute, Troy, NY 12180, USA

Troy, NY 12180 USA; T/F (518) 276-3079/3292; email: zhangxc@rpi.edu

TABLE OF CONTENTS   PAGE

1. Executive Summary

The primary objective of this project is to develop and demonstrate a suitable THz-wave apparatus as a THz imaging platform with a deep sub-wavelength spatial resolution for Army application, potentially for chemical/biological (CB) detection. The spatial resolution of the new T-ray microscopic imaging platform is orders of magnitude greater than what is available in a standard free-space T-ray imaging system, with the target of nanometer resolution. This allows us to explore the rich spectroscopic signatures of hetero-structure, quantum dots, devices and IC circuit diagnostics and molecular vibrations, rotations, and other low-energy transitions for chemical/biological sensing and imaging applications.

During the period of this research, the major activities and achievements are in three areas: THz-wave emission microscope, THz near-field microscope using taper waveguide, and THz photonic devices for THz spectroscopy system. The detailed results and achievements are discussed below for these three research areas.

A novel THz emission microscope has been constructed and demonstrated with ultra-high spatial resolution. A detailed model has been established to explain experimental results and to obtain a clear understanding of the mechanism of the system. A lateral spatial resolution as high as 1 nm has been demonstrated experimentally, and spectral range of the system has been extended from 0.1 to 2 THz. An isolation platform has been built to host the THz microscope, where a 2-D imaging system has been constructed with a step resolution of 0.2 nm. Spectroscopic imaging of a variety of nano-scale objects have been successfully obtained, including hetero-structure interface, nano quantum dots, minute metallic gratings and nano-size GaAs wells.

Using a totally different approach, we have successfully designed, fabricated and tested a new near-field terahertz (THz) microscope apparatus. This method is based on tapered waveguide devices made out of silicon wafer. The tapered waveguide compresses the THz wave quasi-adiabatically to less than $1/10^{th}$ of the THz wavelength, and at the same time functions as minute sample cells. Different from previous apertured techniques, this method can achieve enhancement of THz transmission power through the adiabatic process while keeping the same superior sub-wavelength resolution. Furthermore, since standard silicon processing and fabrication techniques are employed, this method can be extended for mass production. This, in

combination with the requirement of only trace amount of sample for each cell, makes it possible to be employed in industrial testing of chemicals and biological materials through automated testing.

Finally, we have employed a micro-fabrication technique to fabricate novel silicon photonic devices as THz components, such as broadband anti-reflection of THz waves and THz filters. We report the design, fabrication and demonstration of silicon-based devices for reflection reduction and transmission enhancement of broadband THz electromagnetic waves. Anti-reflection effect is achieved in the broad frequency range of 0.2 THz to 3.15 THz using silicon micro-pyramid structures as the AR devices. We observe a maximum 89% reduction in reflectivity of THz power when the sample with 60-μm-period micro-pyramids is used, compared with the reflectivity of a planar silicon substrate. By varying the period of the micro-pyramid devices from 110 µm to 30 µm, the cut-off frequency of enhanced transmission is tuned from 0.74 THz to 2.93 THz and the bandwidth of enhancement increases from 0.91 THz to 3.15 THz, respectively. Although the structures have been demonstrated as anti-reflection devices for silicon substrate, this design can be also used for other substrate materials. Furthermore, the silicon devices also function as low-pass filters.

2. Project Background

Terahertz (THz) waves, lying between infrared and microwaves in the bands of the electromagnetic spectrum, offer innovative imaging and sensing technologies for applications in material characterization, microelectronics, medical diagnosis, environmental control and chemical and biological identification [1,2]. Recent advances in THz science and technology make it one of the most promising research areas in the 21st century for sensing and imaging, as well as in other interdisciplinary fields [3-8]. Combining photonics and scanning near-field microscopic technology in the nano-world leads to new applications from surface science to biophysics [9-12].

2.1 Problem identification

It is well known that an isolated atom has its specific resonance energy levels described as discrete lines by the atomic spectroscopy. Optical spectroscopy of a hydrogen atom is an example, with its ground state energy at 13.6 eV and other excited energy level with an orbital

number n is proportional to ground state energy multiplied by$1/n^2$, as predicted by atomic theory. It is also known that a semiconductor crystal, due to the collective effect, has a set of continuous energy bands. An energy gap between the conduction and valence band could be from several eV to nearly zero, and band theory is required to describe the collective effect, such as the phonon energy. However, the experimental measurements are very difficult when the number of atoms within the interaction range from a few to several thousands, even the theories for the single atom or for the crystal could not be applied anymore. The following list in **Table 2.1** shows the approximate diameter scales of some selected targets. Recent developments in nano technology and cold-atom science represent cutting-edge activities in this research field with the extreme scales.

Scale down	Size	Scale down	Size
Human hair	60-120 μm	Semi. devices structure	100 nm– μm
Pollen	10 to 100 μm	Quantum dot	10 to 50 nm
Asbestos fibers	<3 μm	Phonon lattice	2 to 10 nm
Diesel exhaust particles	<100 nm–1 μm	Nano-tubes & Fullerenes	about 5 to 100 nm
Soot	<10 nm – 1 μm	Atoms	1 to 3 Angstrom

Table 2.1: approximate diameter scales of some selected common targets from sub-mm to Angstrom.

Another less developed, less understood area is the THz phenomena in the 0.1 to 10 THz frequency range. DC to GHz is considered the electronics range, with the classical transport as the dominating physics and the waveguide as the typical element for microwaves; the photonic range is approximately above 100 THz, with quantum transition as the dominating physics and lens and mirror as the guiding elements for optics. The science and technology in the THz frequency, which is between microwave and infrared wave, is still in its infancy, compared with its well-developed adjacent bands.

Is it possible to design an apparatus which can be used for both spatial and temporal study with multi-scalable capability? Could such a device be used for measuring the dielectric properties of the target with its size ranging from angstrom to centimeter, as well as for bridging the frequency from the electronic range (MHz-GHz) to the photonic range (>100 THz)? A THz-wave Emission Apparatus from the semiconductor surface provides spectroscopic THz wave

imaging from meso-scale to nano-scale, with the targets for single molecular, the hetero-structure interface, nano-quantum dot, ultrafast devices, and multi-level IC circuit diagnostics, etc.

2.2   Issue and challenge

Due to the long wavelength of THz waves (300 μm @ 1 THz), the imaging resolution with THz waves is usually limited by diffraction, restricting the multi-scale application, especially in the nano-scale. Small objects with a deep sub-wavelength size are difficult to study by far-field method in the THz frequency range. They are either indistinguishable from the surrounding object within the background or have too small of a reaction cross-section under the THz field. The near-field method has been a powerful technology in breaking down the diffraction limit. Applying the near-field method to the THz frequency range has enabled us to obtain microns or even sub-micron resolution. However, improving the spatial resolution to nanometer or sub-nanometer is the major challenge.

2.3   Technical approach

2.3.1   Aperture-less THz emission microscope

An aperture-less scanning near-field microscope, which uses a sharp tip to scatter the evanescent light in the near-field region of the target to make it detectable in the far field, provides a spatial resolution well below the diffraction limit. Recently, aperture-less near field imaging methods have been applied to construct THz wave microscopes, including use of the tip disturbed local THz field [13] and measurement of the absorption and scattering of THz field by the tip-sample interface [14]. A resolution of 150 nm was reported by measuring the THz wave coupling to the tip-sample system [15].

In our approach, a THz-wave emission apparatus was designed and constructed. It used a pulsed laser to generate photo-carriers on the semiconductor surface and a biased electrode (such as scanning-tunneling-microscope needle) to modulate the localized electric field in the Schottky barrier under the electrode. The transient photo-carriers driven by the modulated field emit a THz wave, which can be detected at the modulated frequency in the far field.

2.3.2   Apertured THz near-field microscope

In addition to the aperture-less near-field microscope, THz imaging in the near-field has been realized with the help of some form of aperture. Either metal apertures or a dynamic optical

beam can be used to reduce the size of the modulated THz beam so that the spatial resolution can be greatly improved. The object can be placed either immediately before or after the aperture to avoid diffraction and achieve near-field effect. Employment of the near-field technique has two advantages: higher spatial resolution and reduction of required sample amount. The spatial resolution of the near-field THz technique is mainly decided by and comparable to the size of the aperture used.

Features with a size of below 1 micrometer can be readily fabricated in the clean room. Silicon, especially high-resistivity silicon, is a material that is very transparent to terahertz waves with extremely low absorption. Use of silicon as a substrate for THz applications is ideal. We achieve the fabrication of periodic, minute trenches on the silicon surface with different diameters and depths. Each trench can be filled with different chemicals and materials. The rest of the silicon surface is coated with a thin metal layer to block other parts of the THz wave so that the THz wave can only transmit through the trenches to achieve high spatial resolution. A thin metal plate with an aperture which has a size larger or comparable to the diameter of the trenches is employed to allow transmission of the THz wave through one trench. As a result, samples in one trench will be measured at a time. Moreover, it is possible to achieve parallel processing if multiple THz detectors can be employed simultaneously. Automation of measurements can be realized by switching samples using motorized stages. As a result, a large variety of samples can be measured in a short period of time, making the system attractive for real-world applications.

3.   THz Emission Microscope

3.1   Experimental setup

A THz emission microscope system uses a pulsed laser to generate photo-carriers on the semiconductor surface and a biased scanning-tunneling-microscope (STM) needle to modulate the localized electric field in the Schottky barrier under the tip. The transient photo-carriers driven by the modulated field emit a THz wave, which can be detected at the modulated frequency in the far field. **Figure 3.1** is the schematic set-up of the scanning THz emission microscope. A femtosecond Ti:sapphire laser with pulse duration of about 10 fs illuminates the semiconductor surface at the Brewster angle. The area of the elliptical laser spot on the semiconductor is approximately 0.5 mm^2, the average optical power is about 50 mW. In a vibration-isolated environment, a STM needle with a tip diameter of 40 nm is brought to the

laser spot via a piezoelectric stage. High mechanical stability in the tip is crucial, and achieved by using a feedback loop to monitor and control its position. The tip is biased with both DC and AC voltages with amplitudes V_{DC} and V_{AC} ranging up to several volts.
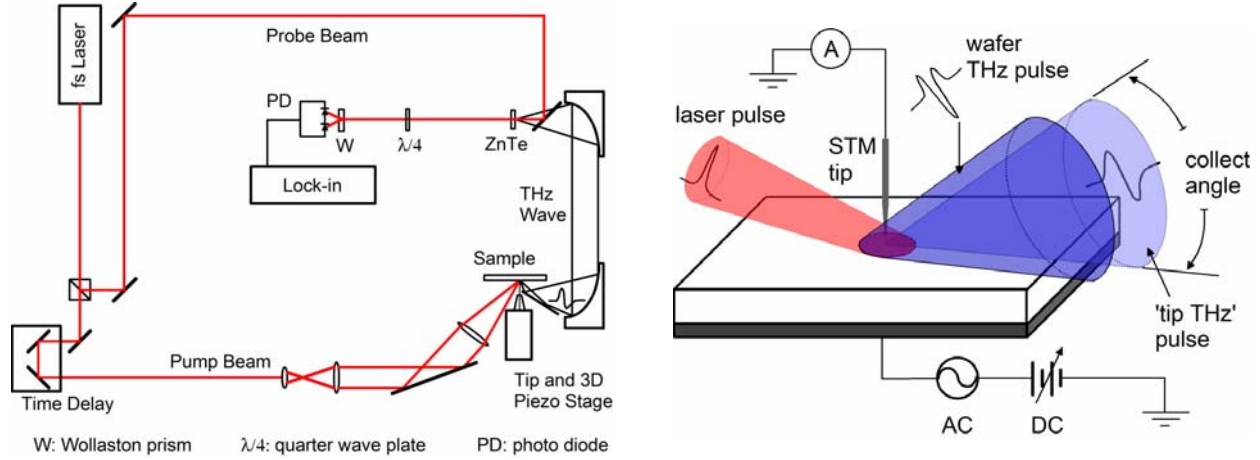

Fig. 3.1 (a) Schematic setup of a THz emission microscope; (b) scanning head of the microscope

3.2   Theory of THz emission microscope: Resonant antenna model

When the tip is moved into the tunneling junction of the sample or is in contact with the sample, a Schottky junction forms below the tip. A depletion (or accumulation) region is built up around the contact point and an electric field is formed due to the presence of net charges. When the Schottky junction has been excited by a transient laser pulse, photo-induced free carriers will be generated and a transient current will be stimulated under the influence of the electric field in the depletion/accumulation region, which can change the balance of the electric field in turn. If there is a bias voltage applied between the tip and the semiconductor, it will modify the potential and electric field distribution in the Schottky barrier as well as the depth of the depletion spot. Consequently, it will modify the THz pulses generated from the Schottky barrier.

The area of depletion (accumulation field) region that is involved in THz generation is of the same order as the tip size (10s nm in diameter). As known from previous results, if the source size for THz generation is much smaller than the THz wavelength, THz radiation efficiency is greatly reduced. Fortunately, the tip wire is in series with the semiconductor depletion region and has the same transient current. Therefore, it functions as an antenna with mm length, which greatly increases the radiation efficiency. The detailed numerical calculations and physical pictures follow.

8

First, we consider the antenna at static condition (i.e. before incident optical pulse breaks the balance):

$$I_{static}(\omega) \propto V/(R+j\omega L - j(\omega C)^{-1}),\tag{3.1}$$

where V is the external bias potential, R is the input resistance of the antenna, L is the tip inductance, and C is the tip-surface capacitance. And the resonance frequency of the antenna is given by:

$$f_{res}=1/(2\pi*sqrt(L*C)).\tag{3.2}$$

The inductance of a straight wire is given by:

$$L=2l(ln(2l/r)-0.75)\ nH,\tag{3.3}$$

where l is the length of the straight wire in cm, r is the radius of the wire, and the unit of inductance is nH.

The capacitance due to the depletion of electrons is given by:

$$C=A*sqrt(q\varepsilon_s N_D/2(V_{bi}-V)),\tag{3.4}$$

where A is the capacitor area, $\varepsilon_s=11.7\varepsilon_o$ is the permittivity of InAs, ε_o the dielectric constant of vacuum, N_D is the donor density, V_{bi} is the build-in potential of the metal-semiconductor junction, and V is the applied bias voltage.

In the current system, the following parameters are used for calculation of L: effective length of the wire is 2.5 mm, effective radius is 1 μm. Then we have L=3.9 nH. For calculation of C, we use an effective depletion radius of 70 nm, donor density of 2×10^{16} cm^{-3}, V_{bi}=of 0.1V, and no external bias. We can derive a C of 2.4×10^{-16} F. Therefore, the resonant frequency of antenna is $f_{res}=1/(2\pi*sqrt(L*C))=0.16\ THz$. This is in good agreement of the 0.18 THz peak frequency obtained from the experiment.

Next, we consider the situation after the optical pulse incident on the semiconductor surface. Transient current, which is caused by the acceleration of photo-carriers in the electric field at the semiconductor surface, is given by:

$$\Delta I_{eff} \propto \mu*E_{eff}*\Delta N+ \mu*\Delta E_{eff}*N\tag{3.5}$$

where μ is the mobility of free electrons in the semiconductor, E_{eff} is the effective electric field in the Schottky field region, and N is the free carrier density, ΔN and ΔE_{eff} are their transient changes, respectively. Then, generated THz field at far-field is given by:

$$E_{THz} \propto \Delta I/\Delta t. \qquad (3.6)$$

The movement of carriers in the depletion region causes a redistribution of carriers, which in turn screens the depletion field. This movement will continue until a new balance is formed between carriers and depletion field. Most of the THz radiation happens at the first stage of interaction, i.e. within the process of generation and initial acceleration.

The experimental results can be successfully explained by this model. Tip THz radiation from InAs is almost one order higher than that from GaAs for p-type semiconductors, because mobility of InAs is higher than that of GaAs. In addition, the absorption length (skin depth) of InAs at 800 nm is about 5 times shorter than that of GaAs. Therefore, the carrier density in InAs is about 5 times higher than that in GaAs. As a result, Tip THz generation from InAs is almost one order higher than that from GaAs. More comparison between experiments and modeling will be made in the following sections.

3.3   Experimental results

There are several possible physical mechanisms, including the transient photo-current, optical rectification, and Photo-Dember effect, that contribute to the generation of THz waves under pulsed optical excitation. When an InAs crystal is used, the major contribution comes from the Photo-Dember effect. Using V_{AC} as a trigger reference for a lock-in amplifier, even with this large THz wave background from the entire laser illuminated area, only the THz wave emitted from the V_{AC} modulated carriers under the tip contribute to the measured THz signal. To distinguish the STM-tip-induced THz signal (below the tip) from the un-modulated THz signal (away from the tip), the modulated THz signal is referred to as the *tip signal*, while the un-modulated THz signal is called the *wafer signal*. The tip signal is collected by a parabolic mirror and detected by the standard electro-optical sampling method [16]. Scanning of the tip is achieved either by moving the tip on piezoelectric stages with a relatively small step size (minimum step of 0.2 nm with a travel range of 6 μm) or on mechanical stages with a larger step size (minimum step of 100 nm with the travel range 10 mm).

When a STM tip comes into contact with the semiconductor surface, the work function difference between the metal and the semiconductor forms a semi-spherical Schottky barrier with a built-in field in the depletion region. As a femtosecond laser generates photo-carriers, an electric dipole oscillation induced by this Schottky area emits the THz wave. The metallic tip couples with the oscillating dipole and enhances the emission via an antenna effect. If a bias voltage V_{DC} or V_{AC} is applied between the metallic tip and the semiconductor surface, it modifies the depletion field and the depletion depth near the Schottky contact. The THz waveform from this highly confined Schottky contact provides a description of the transient carrier dynamics controlled by the external bias. Due to the differences of permittivity, doping density, Schottky potential and carrier mobility among different semiconductor materials, the tip signals generate different THz field transients. This unique property can be used to distinguish different components in semiconductor hetero- or quantum structures.
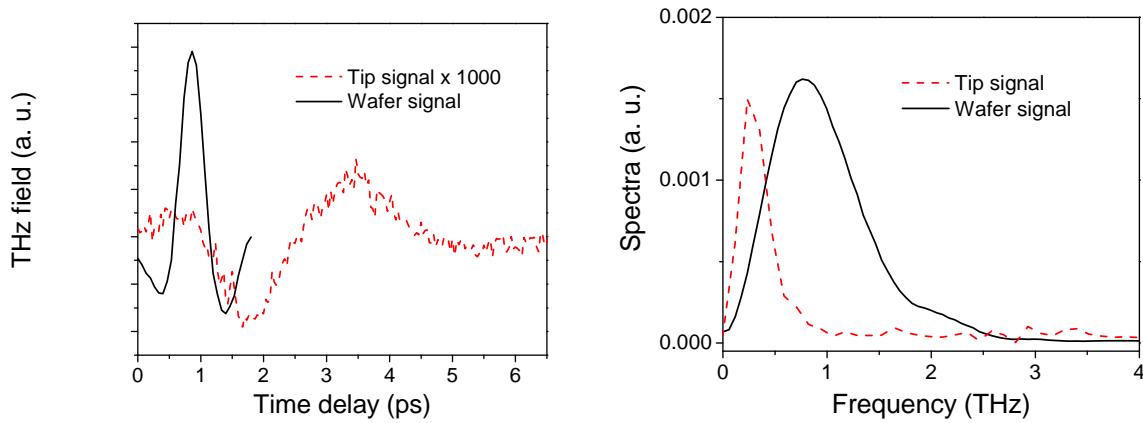
Fig. 3.2 Wafer signal and tip signal obtained from a p-type InAs sample.

Among all the unbiased semiconductors (we tested over 500 samples), a p-type InAs wafer ($1 \times 10^{16}/cm^3$) shows the most intense THz radiation with optical excitation from a Ti:sapphire laser oscillator. Therefore, it is used for most of our studies. As shown before, our model has explained the lower peak frequency of THz waves emitted from the STM tip, and peak frequency shifts from 1 THz of wafer signal to 0.16 THz of tip signal. In addition, there is a time delay of about 0.86 ps between wafer signal and tip signal, as shown in **figure 3.2**. In the previous calculation, we assumed that the area that participates in THz generation has a radius of 100 nm and the focus of laser beam is about 100 μm. The ratio of photo-generated carriers that participate in THz generation is about 10^6: 1. THz field amplitude should scale up with the same

ratio. But tip THz signal is reduced by only 1000 times compared with wafer signal. This indicates the enhancement of antenna effect for THz radiation.

Further proof of the validity of the resonant antenna model is shown in **Figure 3.3**. Tip THz signal is found to strongly depend on the tip shaft length. The temporal position of THz peak is shifted, and the peak frequency of the spectra changed from 0.18 THz to 0.26 THz. This can be explained very well by the antenna model. The temporal shift of THz peak position is proportional to the length of tip shaft. The THz peak frequency shift ratio from experiment is: 0.26:0.18=1.45. This is very close to the theoretical value of 1.4 obtained from equation (3.2), where we calculate the change of inductance as the tip length changes.
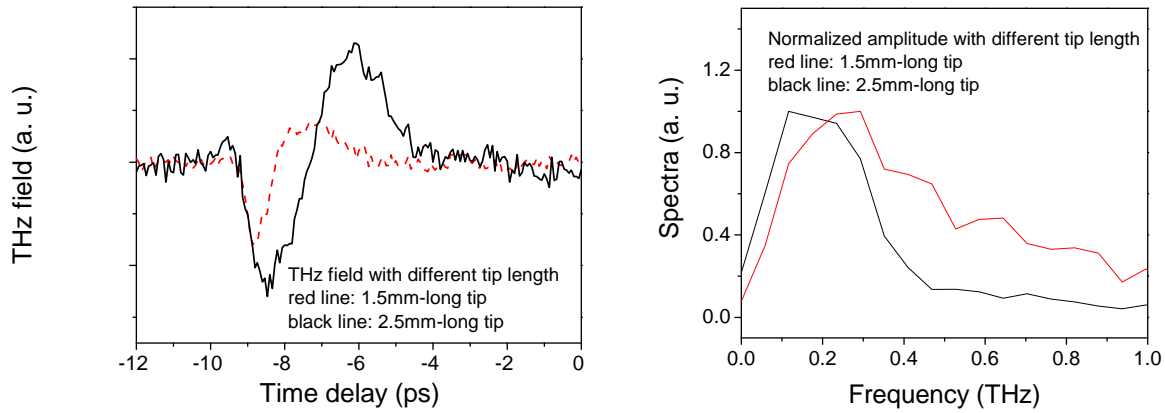
Fig. 3.3 Tip THz waveforms and their spectra obtained at two tip lengths.

The lateral resolution of the microscope is demonstrated by scanning the tip across the edge of a Cr/Au film deposited on the p-type InAs wafer. The average thickness of the metal film is 25 nm. Measurement with an atomic force microscope shows that near the edge, the thickness of the metal film gradually changes to 0 over a 100 nm range. Once the tip makes contact with the metal film, there is no tip signal because a pure Ohmic contact is formed. The peak amplitude of the waveform is plotted in **Figure 3.4**(a). While **figure 3.4**(b) shows the tip signal waveforms during the scan at 1 nm step across the edge of the metal film. Within 1 nm, a sharp change of the tip signal is observed from the InAs/metal interface. Repeating the procedure, we measured the tip signal on an InAlAs/InP interface where 1-μm thick InAlAs is grown on a semi-Insulating InP substrate. At the InAlAs/InP hetero-junction, a transition of the tip signal within 2.5 nm is observed. The demonstrated lateral resolution is much smaller than the size of the tip. Even if the tip size is 40 nm, THz wave emission shows a lateral resolution of 1 nm, which is approximately

1/1,000,000 of the central wavelength of the emitted THz pulse. The transition range is within a few InAs lattice constants. To further increase the spatial resolution, stabilization of the tip within a few Angstroms under laser illumination needs to be accomplished.
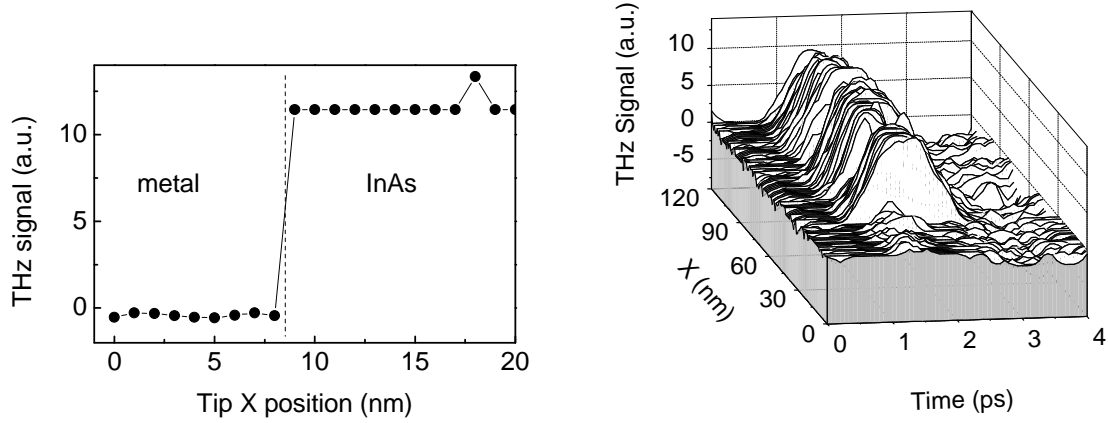

Fig. 3.4 Tip signal as the tip scans across the edge of a metallic layer on an InAs wafer. a: The peak THz amplitude versus tip position across the interface. A sudden drop of the tip signal within 1 nm is observed. b: The temporal waveform of the tip signal as the tip scans across the Au/InAs interface. All waveforms are bipolar. The scanning step size is 1 nm.

If the tip contacts a semiconductor wafer area where there is a metallic layer with an Ohmic contact (linear current-voltage relationship), a moderate AC bias does not modify the surface field, and no tip signal is observed. **Figure 3.5** shows a 2D image (50 μm x 50 μm) of a Cr/Au grating structure deposited on a p-type InAs wafer. The period of the grating is 16 μm with the metallic line width equal to 6 μm. The scanning of the tip is performed using a feedback control with constant contact current mode to maintain tip contact with the target during the scan. The scanning step size is 100 nm across the grating and 500 nm along the grating.
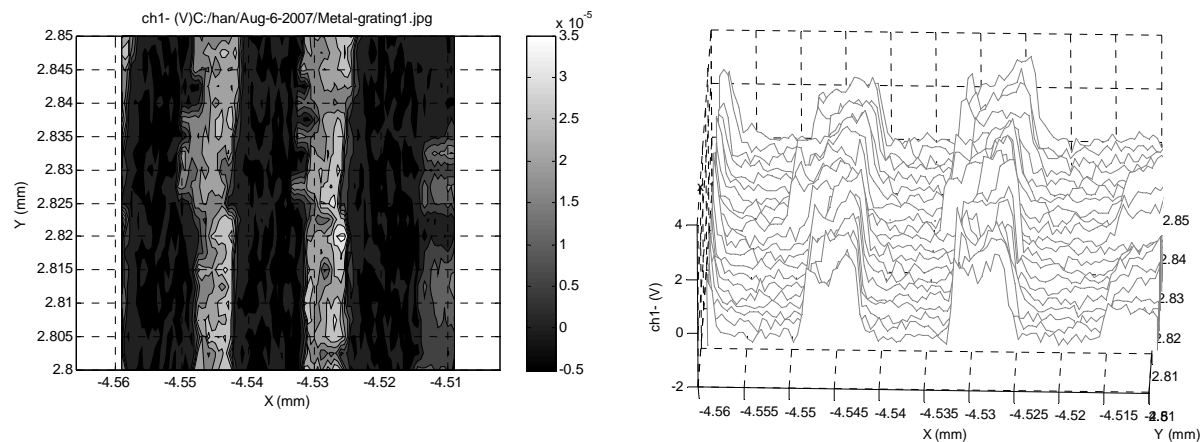
Fig. 3.5 2-D image of a gold grating on InAs substrate.

Quantum dots have very different properties, compared with its bulk counterpart. To further illustrate the application of the microscope, a quantum dot sample (InAsSb quantum dots on InGaAs/InP substrate) is scanned and shown in **Fig. 3.6**. The sizes of the quantum dots are between 20 and 50 nm. Clear contrast between quantum dots and semiconductor substrate is observed.
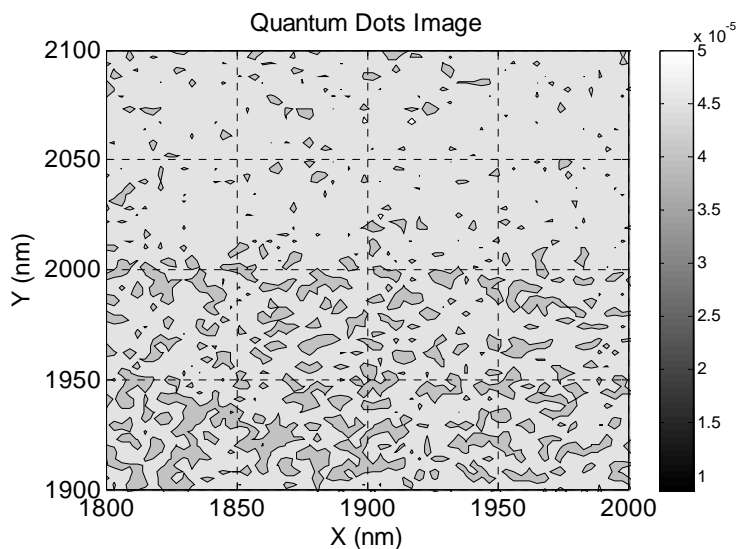

Fig. 3.6 2-D image of InAsSb quantum dots.

3.4   Perspective

In comparison to all other THz wave microscopes, which measure the scattering/absorption of the incident THz wave, this field-controlled THz wave emission uses optical pulse excitation to inject free carriers and a STM tip to modulate surface electric field. As a result, the measured THz wave has zero background and a higher contrast ratio, which is especially important for spectroscopic imaging applications. THz wave radiation has been generated from the materials in the solid [17], liquid [18], gas [19], and plasma phases [20]. A THz emission microscope with a STM tip could help to investigate the dynamics in these materials with nanometer scale resolution.

The THz emission microscope provides a new tool to study the properties of semiconductor materials at nanometer scale. The emission spectroscopy provides the local dielectric property of semiconductor quantum structures, such as the band structure, and transient carrier dynamics. It has the potential to study the electric field distribution as well as the THz frequency response of electrons in high-speed semiconductor devices. Another possible application is the study of optically induced reactions, such as photo-excited electron exchange in molecular scale. THz emission microscopy paves the way toward THz wave spectroscopic imaging of materials and devices at nanometer and sub-nanometer scales.

Carbon nanotubes have been the subject of heavy research in recent years. It has been proposed to use carbon nanotube for applications in ultrafast IC circuit at GHz to THz frequency range. **Fig. 3.7** (a) shows a scanning electron micrograph image of an array of carbon nanotubes. The tubes have a diameter of about 10 nm and a separation of about 50 nm between adjacent nanotubes. THz emission microscope is an ideal tool to study single carbon nanotube because of its high resolution and high frequency. Furthermore, the carbon nanotube shows a resonant absorption peak at THz frequency, as we have shown in **Fig. 3.7** (b). This makes it more interesting to study carbon nanotube using the THz wave microscope.
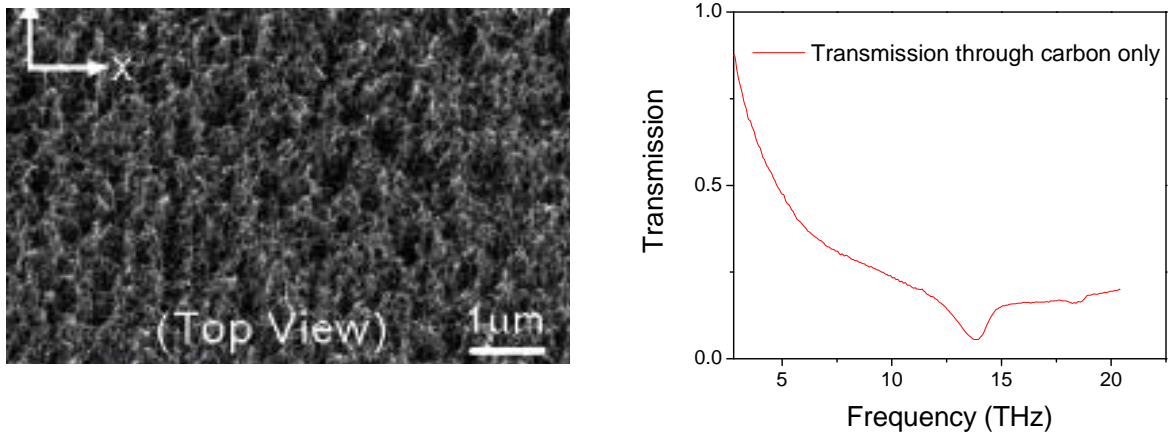
Fig. 3.7 SEM image of carbon nanotubes and its resonant absorption peak at THz frequency.
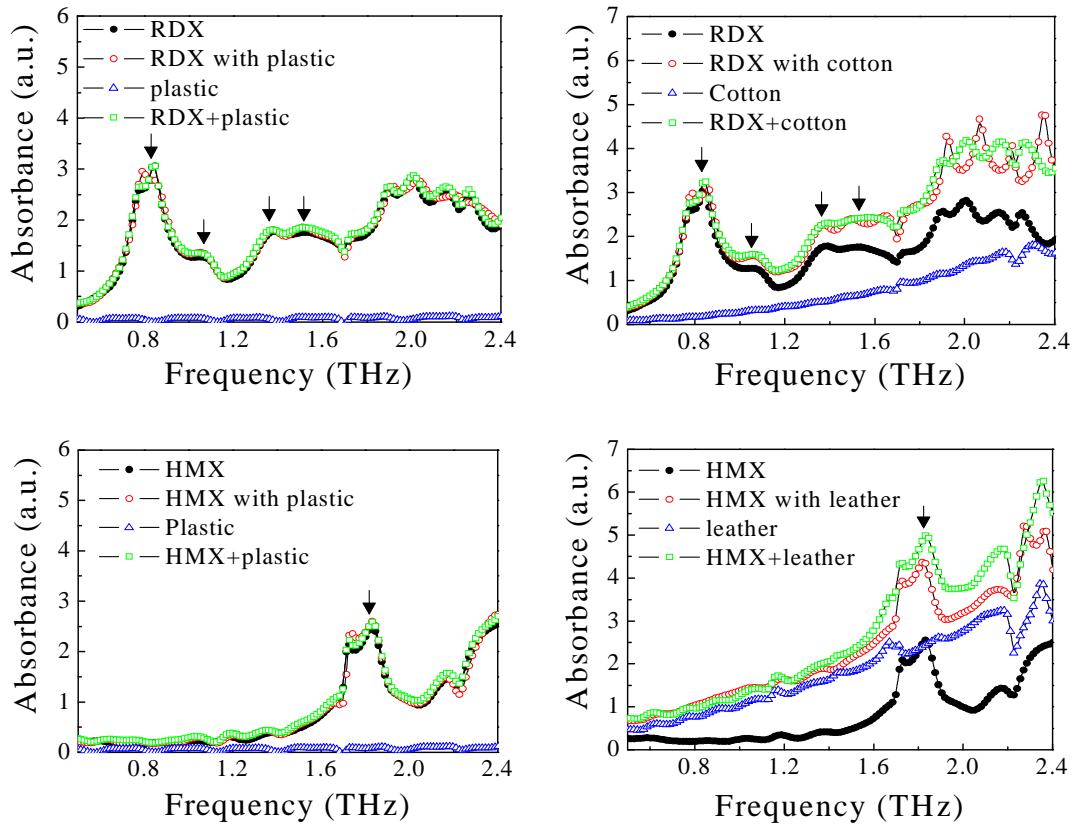

Fig. 3.8 The absorption spectra of RDX and HMX covered with different materials (plastic, cotton and leather). Black solid circle: the transmission spectra of pure samples; red hollow circle: the transmission spectra of covered samples; blue hollow triangle: the transmission spectra of covers; green hollow rectangle: the sum of pure samples and covers.

THz waves can penetrate through many daily-used materials, such as clothing, paper, plastics, leather, wood, and ceramics. Owing to these advantages, THz spectroscopic imaging technology is a competitive method for security screening.[21,22] Recently, we have demonstrated detection of explosives under cloth, leather and plastic, and the explosives have been clearly identified, as shown in **Fig. 3.8**. However, for real application, the resolution of conventional THz imaging, which is at about mm scale, cannot satisfy the requirement of security scanning in certain cases. THz scanning near-field microscopic imaging with higher resolution will be able to solve this problem.
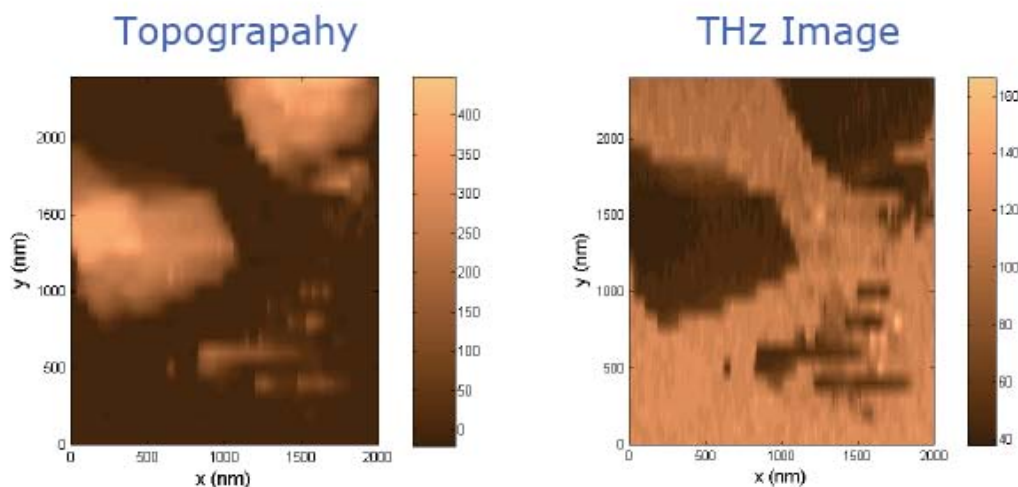
Fig. 3.9 Topographic and THz image of bio-molecular nanoparticles (courtesy of Prof. H. Han, Pohang University of Science and Technology).

Low energy of THz photons enables THz technology a nondestructive/noninvasive sensing method. Many solid chemical/biological materials have THz absorption fingerprints, which are from torsion vibrations, intermolecular (crystalline lattice) vibrations, or hydrogen-bonding stretches. THz spectroscopy has recently been applied in the investigation of many chemical compounds, pharmaceutical materials, illegal drugs, amino acids, nuclei-bases and bacterial spores, etc. Recently, biomolecular nanoparticles have been successfully imaged using a THz microscope by the group of Prof. Han at Pohang University of Science and Technology, as shown in **Fig. 3.9**. This once again shows the probability of the application of THz microscope in nanometer size biomolecular or even single molecular imaging. A modified tip could be employed. A nano-particle would be coated with a chemical or biological nano-layer or

even a mono-layer. The nano-particle could be made of metal or graphite, and would be attached to the tip of the THz microscope. Electrical and THz property of the chemical/biological coating layer would be studied. The advantage of this approach is that there is no need to search for the location of the nanoparticle, and at the same time, nanometer resolution is guaranteed.

4.   Apertured THz Near Field Microscope

Under the support of this fund, we have successfully designed, fabricated and tested a new near-field terahertz (THz) microscope device. This method is based on tapered waveguide devices made out of silicon wafer. The tapered waveguide compresses the THz wave quasi-adiabatically to less than $1/10^{th}$ of the THz wavelength, and at the same time functions as minute sample cells. Compared with previous apertured techniques, this method can achieve enhancement of THz transmission power through the adiabatic process while keeping the same superior sub-wavelength resolution. Furthermore, since the standard silicon processing and fabrication techniques are employed, the technique can be extended for mass production. This, in combination with the requirement of only trace amount of sample for each cell, makes it possible to be employed in industrial testing of chemicals and biological materials through automation.

4.1   Motivation and background

THz waves, like infrared and microwaves in the adjacent bands of the electromagnetic spectrum, offer innovative imaging and sensing technologies for applications in homeland security, material characterization, microelectronics, medical diagnosis, environmental control and chemical and biological identification. However, the spatial resolution of a THz imaging system is usually limited by diffraction to be in the order of its wavelength at far field. This level of resolution is inadequate to identify semiconductor circuits, biological cells and other applications involving minute objects. To overcome the spatial resolution limitation, two types of methods are employed: apertured near-field microscope and aperture-less near-field microscope.

Apertured near-field microscope traditionally uses an aperture cut out of a metal film. The film blocks THz waves other than the THz wave at the aperture outlet. At near field, the spatial resolution is comparable to the aperture dimension. However, the throughput of the THz through the minute aperture is extremely small, reducing the system dynamic range severely. As a result, the aperture size is usually in the order of a few microns.

On the other hand, an aperture-less scanning near-field microscope, which uses a sharp tip to scatter the evanescent light in the near-field region of the target to make it detectable in the far field, provides a spatial resolution well below the diffraction limit. Recently, aperture-less near-field imaging methods have been applied to construct THz wave microscopes, including use of the tip-disturbed local THz field and measurement of the absorption and scattering of the THz field by the tip-sample interface. A resolution of 50 nm was reported by measuring the THz wave coupling to the tip-sample system. However, an aperture-less near-field microscope usually detects distorted or scattered THz waves. Because of the scattering nature, geometric arrangement and limited dynamic range, it is difficult to get spectroscopic information using the aperture-less microscope. Moreover, locating tiny samples can be a problem in real-world applications.

In this research, we demonstrate that improved throughput can be achieved by using a tapered waveguide for quasi-adiabatically compressing the THz waves. Preliminary testing shows an enhancement of transmitted power by a factor of 4, compared with the transmitted THz power through an aperture without a tapered waveguide. Unlike flat aperture, transmitted THz power deviates significantly from the expected d^6 dependence on the aperture diameter (d), further indicating that THz transmission through the tapered aperture has been augmented. To characterize the THz field and frequency dependence after transmission through the tapered aperture, THz field after transmission of the tapered aperture has been measured, showing a shift to higher center frequency and reduction of overall amplitude. To better understand the experimental observation, a simulation illustrates enhanced THz field distribution at the near field of the new aperture. This microscope technique has many advantages, such as the high spatial resolution of near-field optics, the easiness to locate samples, the ability to measure a large variety of samples simultaneously, and automation possibility.

4.2   Technical approach: mechanism and design

For an apertured near-field microscope, either metal apertures or a dynamic optical beam can be used to reduce the size of the modulated THz beam so that the spatial resolution can be greatly improved. The object can be placed either immediately before or after the aperture to avoid diffraction and achieve near-field effect. Employment of the near-field technique has two advantages: higher spatial resolution and reduction of required sample amount. The spatial

resolution of the near-field THz technique is mainly decided by and comparable to the size of the aperture used.

Features with a size of below one micrometer can be readily fabricated in the clean room. Silicon, especially high-resistivity silicon, is a material that is very transparent to terahertz waves with extremely low absorption. Use of silicon as a substrate for THz applications is an ideal choice. We have achieved the fabrication of periodic, minute tapered waveguides on the silicon surface with different diameters. The rest of the silicon surface is coated with a thin metal layer to block other parts of the THz wave so that the THz wave can only transmit through the waveguides to achieve high spatial resolution. Each waveguide can be filled with different chemicals and materials. Moreover, it is possible to achieve parallel processing if multiple THz detectors can be employed simultaneously. Automation of measurements can be realized by switching samples using motorized stages. As a result, a large variety of samples can be measured in a short period of time, making the system attractive for real-world applications.

To achieve a micron-size waveguide-based THz near-field apparatus based on the silicon fabrication process, a wet etching technique is employed to obtain opening about 5 microns in silicon substrate, as shown in **Fig. 4.1**. Pyramid-shape tapered waveguides have been fabricated out of silicon, and gold metal film deposited onto the wall of the waveguide to form the THz waveguide and increase THz throughput. The output aperture (Wo) is continuously tunable from under 5 microns to 100 microns by controlling etching time and etching rate, as shown in **Table 4.1**. This near-field apparatus can be used in near-field imaging and spectroscopy. Furthermore, because silicon is a very mature material for nanoscale fabrication and mass production, this technique can find potential applications in large-scale fabrication and testing of biological samples.
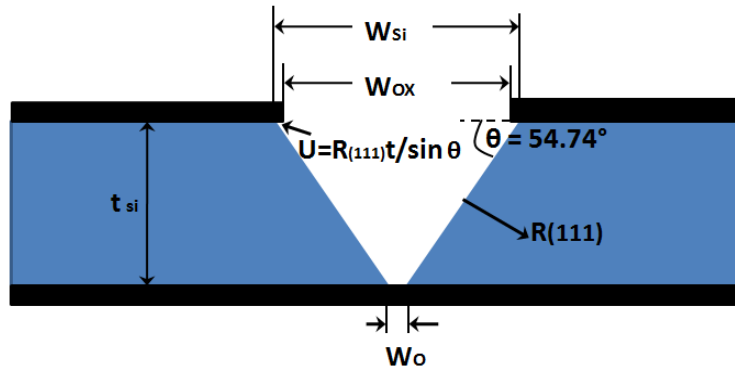

Fig. 4.1 Schematic fabrication process of a THz tapered waveguide for near-field THz microscope.

W_0 (µm)	5	10	20	30	50	100
W_{Si} (µm)	542.4	547.4	557.4	567.4	587.4	637.4
U	63.3					
Wox	415.8	420.8	430.8	440.8	460.8	510.8

Table 4.1 opening (W_0) and base (W_{si}) of tapered waveguides under fabrication.

One distinctive advantage of using this type of tapered THz waveguide is the enhancement of THz intensity at the exit through quasi-adiabatic compression and much improved spatial resolution. Furthermore, the amount of sample required is greatly reduced, which is very cost-effective for industry applications.

4.3   Finite element method simulation

It has been shown theoretically that adiabatic compression of THz waves down to sub-micron size can enhance THz intensity by 10 – 250 times.[23] The principal limits for the nano-concentration of THz waves in metal/dielectric waveguide and determination of the optimum shapes have also been established. In order to better predict the performance of tapered waveguides for near-field application, we have employed the finite element method (FEM) to simulate electric field distribution at the output aperture of the tapered waveguide. In our simulation, the input region is set up as a rectangular box and the output region is set up as a semi-sphere. The tapered waveguide structure is sandwiched between these two regions, with an input opening of 540 µm and an output aperture of 6 µm. This simulation setup is shown in **Fig. 4.2** and **Fig. 4.3** in 3-D view and x-y cross-section view, respectively.

The simulation frequency is set at 0.2 THz. A plane wave is set up to propagate in the y-direction. Mesh size is five times smaller than the simulation wavelength. With convergence set at 1e^{-8}, **Fig. 4.4** and **Fig. 4.5** illustrate the electric field distribution of the simulated structure.
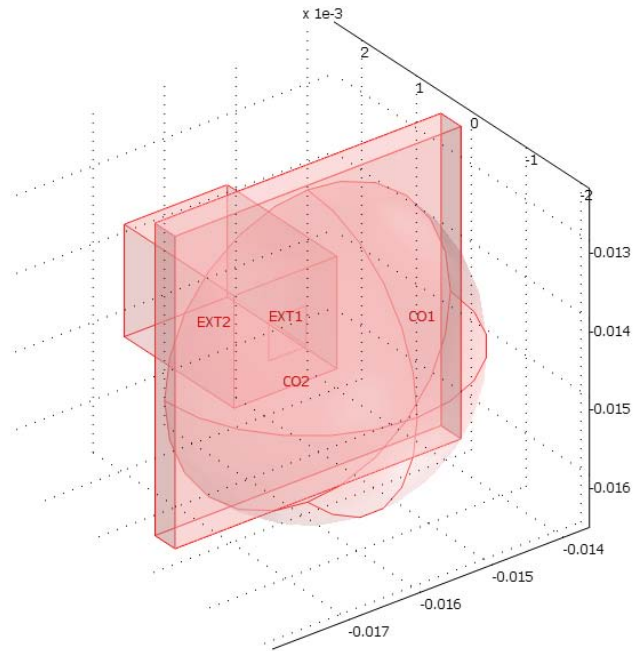
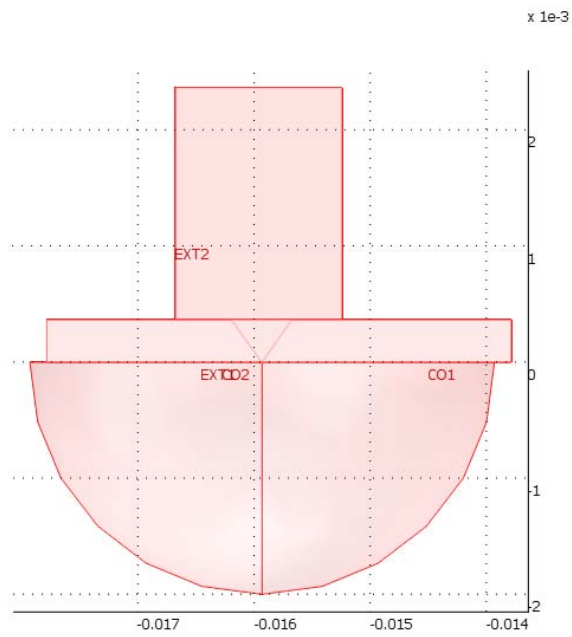**Fig. 4.2** 3D geometrical setup of a tapered waveguide for FEM simulation.

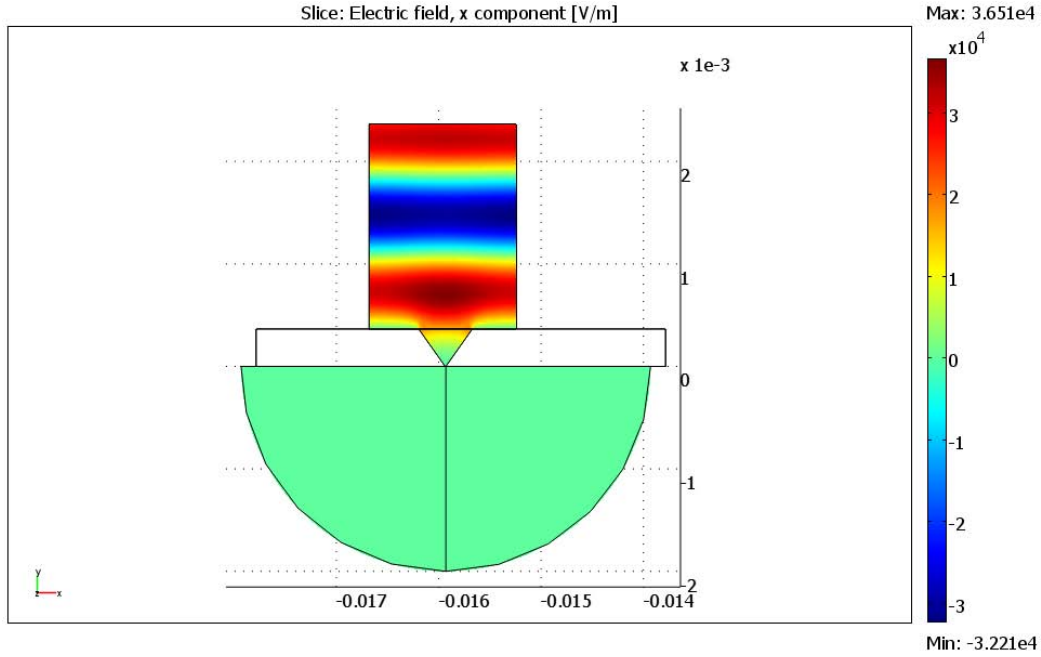**Fig. 4.3** Cross-section view of the geometrical setup of a tapered waveguide for FEM simulation.

Fig. 4.4 FEM-simulated x component of THz electric field of the whole simulation system at 0.2 THz.
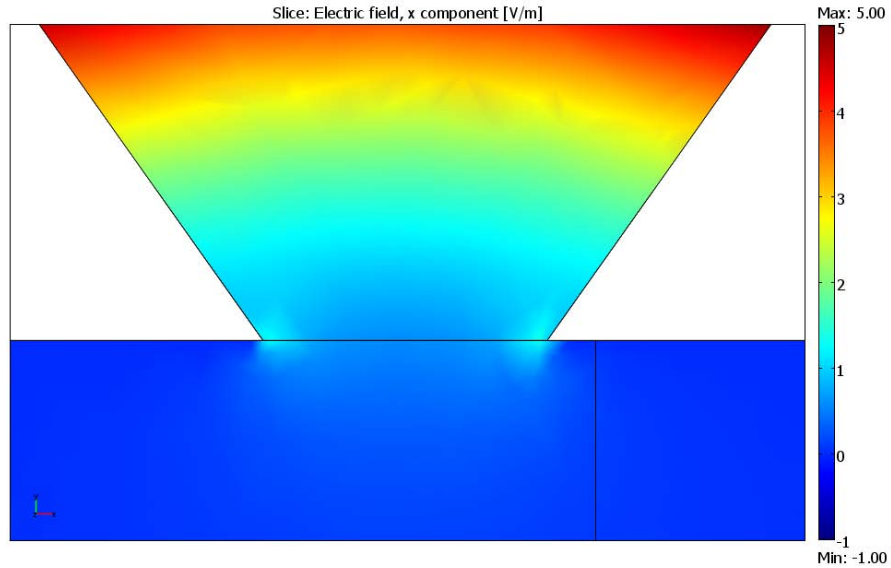

Fig. 4.5 FEM-simulated x component of THz electric field near the exit of the tapered waveguide at 0.2 THz.

4.4   Fabrication of tapered waveguides

Fabrication of a micron size device with desirable shape is quite challenging mechanically. Use of lithography fabrication method makes it much easier to realize this concept. Furthermore, it is of both scientific and practical importance to demonstrate this adiabatic compression of THz field in a tapered waveguide experimentally. We have employed crystallographic wet etch for the fabrication of tapered waveguides. Commercially available 25%

TMAH solution is used with surfactant at 90°C as the etchant. Linear arrays of square openings are defined on the mask layer, in which the etching process takes place. After the etching is completed, a 100-nm thick layer of gold is deposited on the sample by electron beam evaporation. **Fig. 4.6** shows the optical image of the sample after the electron beam evaporation. **Fig. 4.7** and **Fig. 4.8** illustrate the SEM images of a tapered waveguide with a 6-µm output aperture. Since the etching process has some inherit variations, we examined SEM images of various tapered waveguide structures and compared them with the original design to insure the fabrication process is successful. The results are shown in **Table 4.2**.

The sample arrays are composed of tapered waveguides with various diameters and 1-cm spacing. The spacing between trenches is uniform so that it is possible to realize automation measurements and loading and unloading becomes very convenient. It is possible to fabricate waveguides with a diameter from sub-micron to several hundred microns and variable spacing. The choice of waveguide aperture size depends on the samples to be studied. For a smaller one, the spatial resolution is higher and the amount of sample is smaller, but the signal-to-noise ratio is lower due to the low throughput; while a larger one allows a higher signal-to-noise ratio at the sacrifice of spatial resolution and usage of more samples. Usually, samples with high absorption coefficients can be measured in smaller amounts and vice versa.
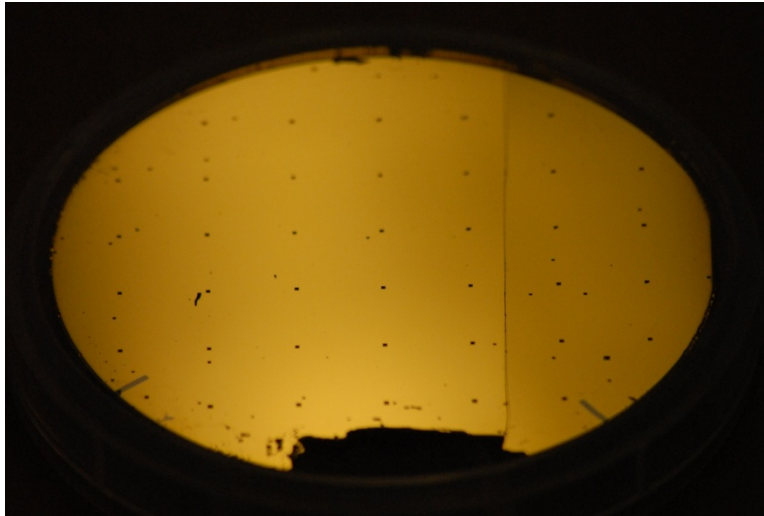

Fig. 4.6 Optical image of a gold-coated silicon wafer with 2D arrays of tapered waveguides.
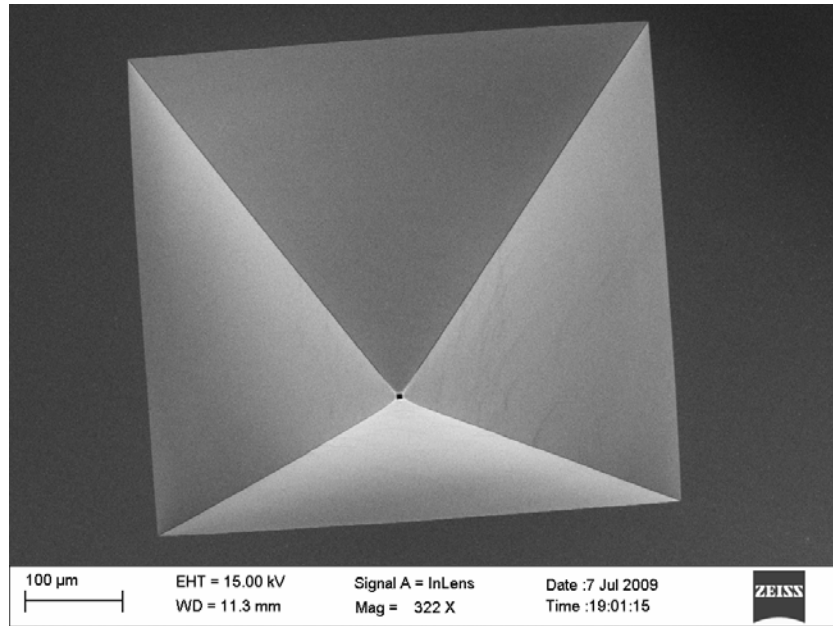
Fig. 4.7 SEM image of a tapered waveguide with an opening of approximately 543 µm and an output aperture of approximately 6 µm.
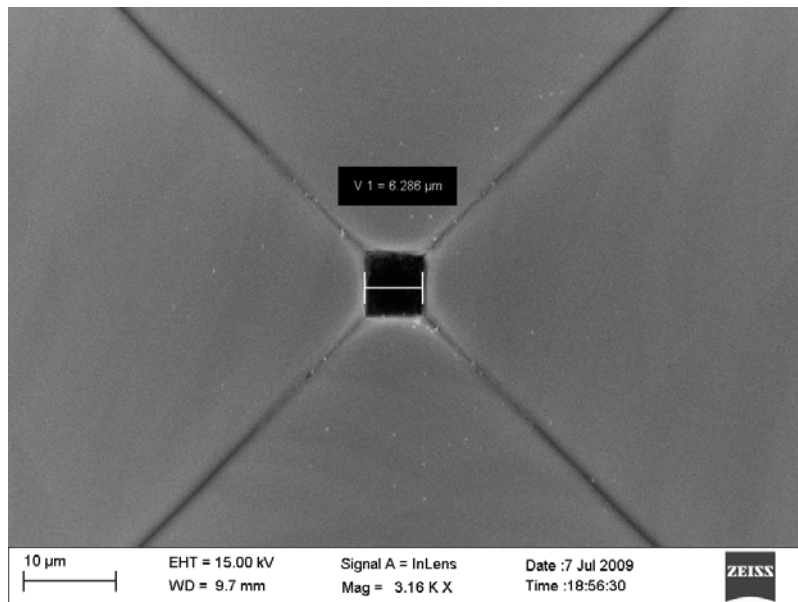

Fig. 4.8 SEM image of a tapered waveguide with an output aperture of approximately 6 µm.

Designed parameters		Actual parameters	
Wo (µm)	Wsi (µm)	Wo (µm)	Wsi (µm)
5	542.4	6.3	544
10	547.4	9.5	551
20	557.4	23	559
30	567.4	31.2	572
50	587.4	52.1	582.6

Table 4.2 Design parameters of tapered waveguide structures and actual parameters of fabricated structures.

4.5   Experimental setup and performance evaluation

Two THz systems have been used to evaluate the performance of the near-field microscope. In the first system, the tapered waveguides are tested with a gas laser and a pyroelectric detector. A CW THz beam at 1.62 THz is collimated from the gas laser and focused by a lens with 16.7-mm focal length onto the opening of the tapered waveguide structure. A pyroelectric detector is positioned as close as possible to the output aperture of the structure to detect transmitted THz power. Output aperture size versus transmitted THz power is plotted in log scale as shown in **Fig. 4.9**. The transmitted THz power has a sub- d^6 dependence on the output aperture size of the tapered waveguides, shown by the fit line in red. We also plotted the d^6 law in dash line along with this set of data. Deviation from the conventional d^6 law indicates that the tapered waveguide does have an enhancement effect on THz transmission.

To verify the enhancement directly, we have compared the power transmission of the tapered waveguides with that without the waveguide. Using the tapered waveguide with 37 µm output aperture, we flipped the structure so that the output aperture now becomes the input opening. The transmitted power of such a setup is four-times smaller than the original setup, which demonstrates THz power enhancement by using tapered waveguides.
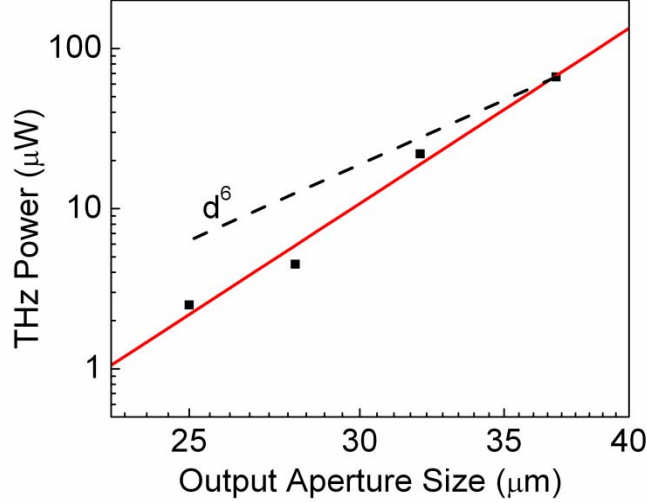
Fig. 4.9 Transmitted THz power (black dot) versus tapered waveguide output aperture size and its fit (red line) compared with d^6 law plot (dash line).

In the second system testing, we tested the tapered waveguide structures using a standard THz-TDS spectrometer. **Fig. 4.10** is a schematic illustration of a T-ray near-field microscope in transmission geometry. A Ti:sapphire laser delivers optical pulses with sub-100 fs pulse width, 80 MHz repetition rate, 800 mW average power and 800 nm center wavelength. THz pulses are generated by photo-carrier transportation at the surface of InAs using a chopper-modulated pump beam. The probe beam, which is split from the laser output, is combined with the THz beam by a reflective silicon wafer, which is transparent to the THz wave. An electro-optic THz detector such as a ZnTe crystal is used to detect THz signals. The waveguide sample is positioned directly in front of the detection EO crystal. Both THz beam and optical probe beam are focused into the waveguide for EO detection. Because the EO crystal is located right after the output aperture of the waveguide, near field detection is realized. If spectroscopic study of materials is needed, the probe beam will be directed from the back of the EO crystal so that it will not be scattered by the material inside the waveguide. This near-field microscope system can be used for both THz sensing and imaging.

Fig. 4.11 (a) shows the THz waveforms without any sample and after transmission through two tapered waveguide structures with different output aperture size of 37 micron and 32 micron. Their corresponding spectra are shown in **Fig. 4.11** (b) with dramatic reduction of THz field at all frequencies. Moreover, it can be seen clearly that the peak THz frequency shifts after transmission. To see the frequency shift more clearly, we plot the normalized THz spectra in **Fig. 4.11** (c). The peak frequency has shifted from 0.8 THz without any sample to 1.4 THz of 37-μm

27

aperture and 1.8 THz of 32-µm aperture. This can be explained by the known law that shorter wavelength (larger frequency) has higher transmission through a sub-wavelength aperture.
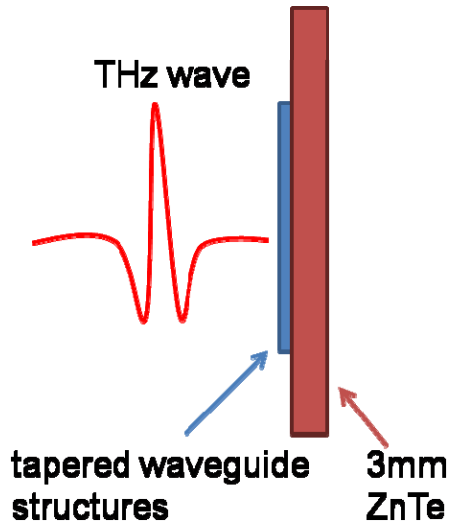

Fig. 4.10 Schematic illustration of near-field THz microscope in transmission mode.
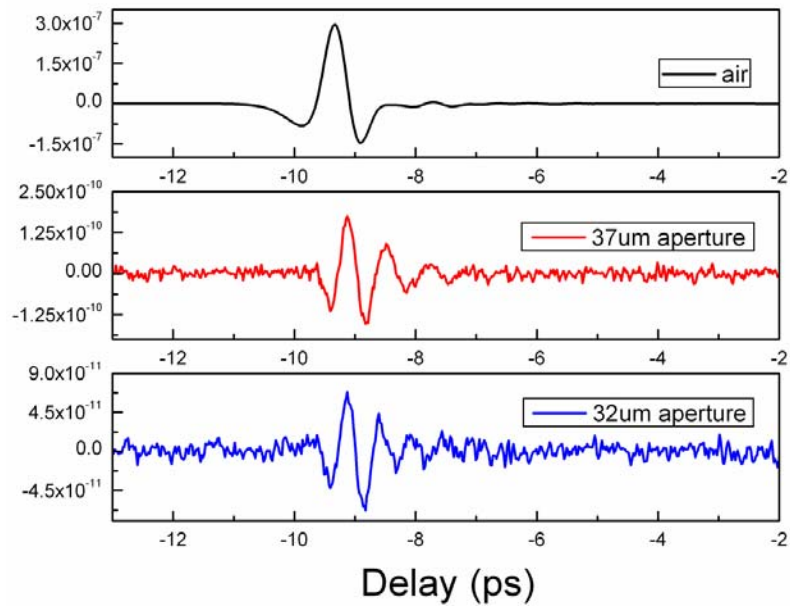

Fig. 4.11 (a) Time-domain waveforms in air, and after transmission through a tapered waveguide with an output aperture of 37 µm and a tapered waveguide with an output aperture of 32 µm.

Fig. 4.11 (b) THz spectra in air, and after transmission through a tapered waveguide with an output aperture of 37 µm and a tapered waveguide with an output aperture of 32 µm.
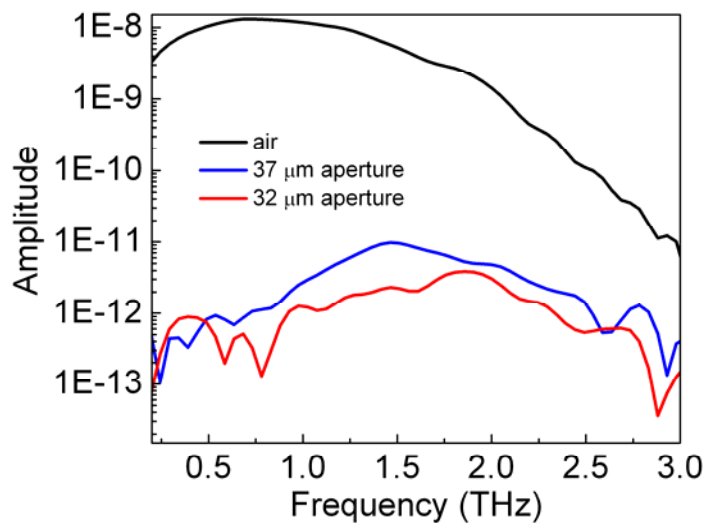

Fig. 4.11 (c) Normalized THz spectra in air, and after transmission through a tapered waveguide with an output aperture of 37 µm and a tapered waveguide with an output aperture of 32 µm.
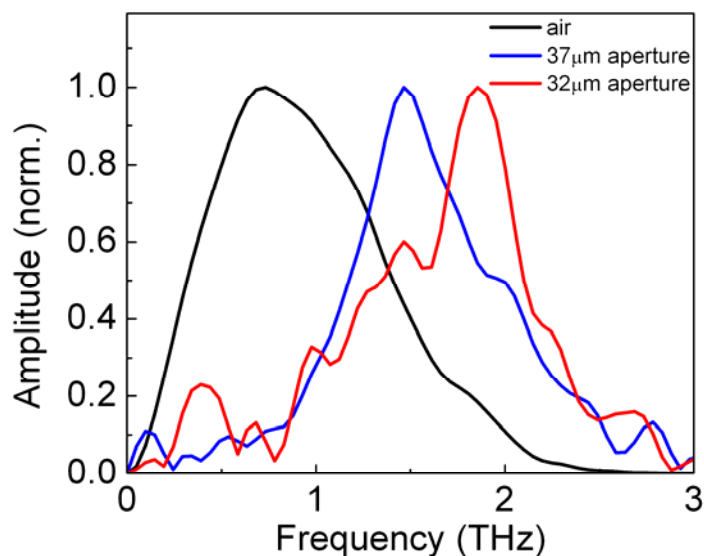
4.6 Perspective

Low energy of THz photons enables THz technology to be a nondestructive/noninvasive sensing method. Many solid chemical and biological materials have THz absorption fingerprints, which are from torsion, vibrations, intermolecular (crystalline lattice) vibrations, or hydrogen-bonding stretches. THz spectroscopy has recently been applied in the investigation of many chemical compounds, pharmaceutical materials, illegal drugs, amino acids, nuclei-bases and

bacterial spores, etc. THz waves can also penetrate through many daily-used materials, such as clothing, paper, plastics, leather, wood, and ceramics. Owing to these advantages, THz spectroscopic imaging technology is a competitive method for security screening. Recently, we have demonstrated detection of explosives under cloth, leather and plastic. These explosives have been clearly identified, as shown in **Fig. 3.8**. However, for real application, the resolution of conventional THz imaging, which is at about mm scale, would not satisfy the requirements of security scanning in certain cases. For example, trace explosives detection is usually necessary in real world applications, instead of bulk material detection. The THz near-field microscope with higher resolution may be able to solve this problem.

In molecular biology, proteomics (protein informatics) is the global study of the collection of proteins produced by an organism, a tissue or a cell type. There are two distinct proteomics fields. One is classical proteomics, which includes the identification of proteins and different protein expressions. The other (and more important), is functional proteomics, which includes the identification of protein interactions. Spectroscopy using a T-ray microscopic instrument as proposed here will provide us with the unique signatures of various proteins in the THz frequency range.

One of the immediate applications is the fast access of T-ray spectroscopy for biochips. Two types of DNA chips now available are based on the principle of hybridization in which nucleotides on complementary nucleic acid strands recognize each other through base pairing. Our proposed technique produces a 'synthesized' DNA or protein chip, comprised of a huge number of oligonucleotide probes that are synthesized directly onto a silicon wafer using photolithography. An automated T-ray microscope can be designed to characterize the next generation of protein biochips.

The T-ray microscope could dramatically enhance pathological inspection and analysis of tissues. In addition to helping with diagnosis, it could even be useful in helping to discover causes of the pathology by showing molecular level information that is linked to morphological changes in the tissue or cells. To realize that, a detailed analysis of specific changes in spectroscopic signatures with subtle changes in molecular structure or composition in the bio-molecules is required. The microscope may also be used to investigate rapid biochemical responses to selected stimuli, giving new insight into biological processes. Future research will see cooperation with biomedical groups on THz spectroscopy of proteins and bio-molecules.

5   Photonic Devices for THz Applications

5.1   Background

THz time-domain spectroscopy is rapidly finding uses in an extremely wide range of applications, from basic science to homeland security, medical imaging and astronomy. Many applications place strict requirements on the performance of THz spectroscopy, including broad bandwidth, high dynamic range and high spectral resolution. Silicon, especially high-resistivity silicon, has become one of the most popular materials for applications in THz spectroscopy as a window, lens, filter or beam-splitter, because it has a very broadband transparent window with little absorption of electro-magnetic waves, spanning from microwave to mid-infrared [24]. However, due to its inherent high dielectric constant, silicon usually is associated with high Fresnel reflection loss, and nearly 30% of THz power will be reflected away at just one air-silicon interface. Furthermore, in time-domain THz spectroscopy, the reflection of THz pulses within silicon components generates multiple pulses at certain time delays depending on the thickness of the components. In order to avoid the Fabry-Perrot interference fringes in spectra from multi-reflection, it is sometimes necessary to use a limited time window and cut the reflected pulses, which in turn limits the spectral resolution. In addition, time-resolved THz spectroscopy is used to study dynamics in the scale of many picoseconds, even nanoseconds, where reflected pulses could smear the obtained waveforms. Since several silicon components may be used in THz spectroscopy, it is of great importance to reduce the reflection at the air-silicon interface, in order to increase dynamic range and improve spectral resolution and system performance.

On the other hand, photonic crystals are becoming very attractive optical materials for controlling and manipulating the flow of light. Photonic crystals are composed of periodic dielectric or metallo-dielectric nanostructures that affect the propagation of electromagnetic (EM) waves in the same way as the periodic potential in a semiconductor crystal affects the electron motion by defining allowed and forbidden electronic energy bands. [25-27] One-dimensional photonic crystals are already in widespread use in the form of thin-film optics with applications ranging from low and high reflection coatings on lenses and mirrors to color changing paints and inks. Higher dimensional photonic crystals are of great interest for both fundamental and applied research, such as photonic-crystal fibers, integrated photonic circuits and even optical computing.

In this work, we have designed, fabricated and demonstrated silicon-based photonic devices for anti-reflection of broadband THz electromagnetic waves. Photolithography and etching techniques of the semiconductor industry are employed for the fabrication of two-dimensional photonic crystals, which are composed of closely-packed two-dimensional periodic arrays of micro-pyramids. The functioning of this photonic crystal is analogous to the moth-eye anti-reflection (AR) structure. Significantly improved impedance matching is realized at the interface between the air and silicon substrate through these AR structures, reducing THz reflection significantly. Furthermore, the AR bandwidth and cut-off frequency can be tuned by varying the size of the micro-pyramids. Finally, this concept can also be utilized for AR of other substrate materials and as a low-pass filter for THz waves.

5.2   Design of AR photonic devices

AR of EM waves can be realized using several different methods, including single-layer interference design, multi-layer design, absorptive AR design and inhomogeneous design (such as moth eye). [28, 29] For application in THz time-domain spectroscopy, absorptive AR devices cannot be used because transmission through THz components is usually necessary.

For single-layer AR coating, several schemes were employed as the AR layer for THz waves. A traditional method was to use a quarter-wave thin film as AR layer which had a refractive index near $\sqrt{n_{silicon}}$ (~1.85), where $n_{silicon}$ is the refractive index of silicon. [30, 31] This method is only suited to enhance transmission of a specific frequency, and is inadequate for broadband THz time-domain spectroscopy. Furthermore, it is hard to find suitable materials with the right refractive index of 1.85 at THz frequency. For example, polyethylene and parylene, which were used in reference 8 and 9, have a refractive index of 1.52 and 1.62, respectively. There are other ways to produce the AR layer other than coating. A photonic crystal slab made with air holes in silicon was also illustrated as a narrowband AR layer between 0.1 THz to 0.45 THz, whose performance at higher frequencies dramatically deteriorated. [32]

The multi-layer coating was more suitable for broadband anti-reflection. Usually, the design and fabrication process is complicated by the lack of materials that have low absorption and suitable refractive index between that of silicon and air at THz frequency. [33, 34] The inhomogeneous AR design offers more versatility and promise. For example, silicon nano-tips were reported as an AR coating layer between air and silicon substrate, whose improvement of

transmission was limited to frequencies higher than 1 THz. [35] However, the distribution of nanotips is somewhat random and it is not easy to obtain a designated refractive index profile. More recently, a sub-wavelength surface relief structure was employed to implement enhanced transmission. [36-39] This method increased zero–order diffraction by utilizing a grating structure smaller than THz wavelengths which was prepared by mechanical ruling or plasma etching.

5.3   Fabrication of AR Photonic Crystals

In this work, we have realized the use of silicon-based photonic crystals as inhomogeneous moth-eye type AR devices. The silicon immersion grating technology, based on lithography and anisotropic chemical etching, is used for the fabrication of AR components. [40, 41] It permits the production of AR structures with a variety of feature sizes from microns to hundreds of microns. Furthermore, it can be applied to the relatively brittle silicon, unlike the conventional ruling techniques. This approach takes advantage of the crystal structure of silicon to form sharp pyramids and very smooth facets through anisotropic etching by certain chemical reagents, e.g. tetramethyl ammonium hydroxide (TMAH). For instance, TMAH attacks the silicon (100) planes much faster than the (111) planes. The pyramids with a large apex angle are formed once chemicals reach the (111) surfaces. The size of the pyramids is determined by the initial mask size.

The process for fabricating silicon pyramids involves the following steps as illustrated by the flowchart in **Fig. 5.1**. The silicon wafer's surface is chemically-mechanically polished to optical flatness. First, a 0.5-µm-thick layer of etching-resistant SiO_2 is grown on a <100> silicon substrate (p-type, resistivity > 15 KΩ-cm) using plasma-enhanced chemical vapor deposition. The substrate with the oxide layer then undergoes the standard UV photolithography process, during which the desired pattern is transferred from the photo-resist to the oxide layer. Once the desired mask pattern is obtained by selectively etching off the silicon oxide, commercially available 25% tetramethylammonium hydroxide with surfactant is used as the etching solution for silicon. The etching recipe is crystallographic as the etch rate in <100> direction is six-times faster than that in <110> direction and 60 times faster than that in <111> direction, which produces square micro-pyramids with an apex angle of 72 degrees formed by four <111> planes.

[40, 41] After the etching is completed, the oxide mask is removed in a buffered hydrofluoric solution.

1. Polished silicon wafer

2. Growth of SiO$_2$

3. Spin on photoresist

4. Pattern by lithography

5. Etching of SiO$_2$

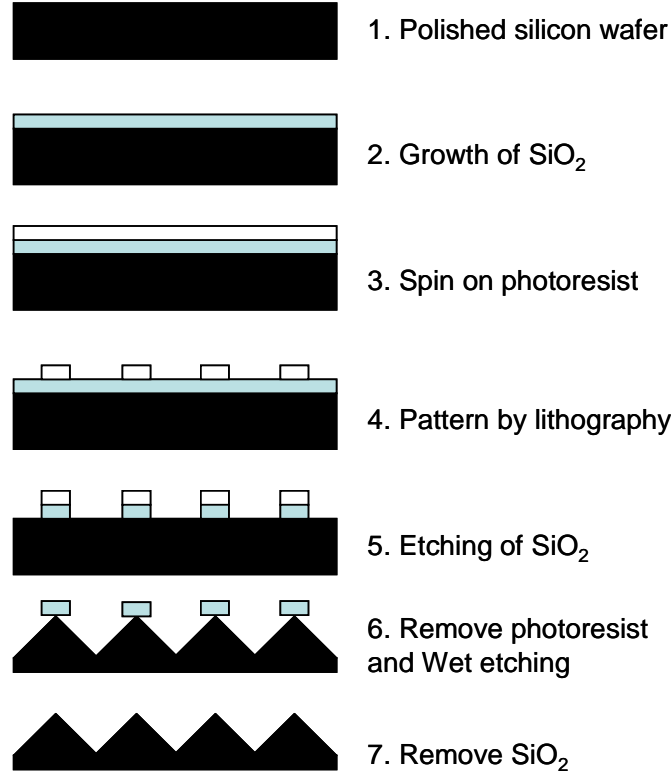**6. Remove photoresist and Wet etching**

7. Remove SiO$_2$

Fig. 5.1 Flowchart of AR photonic crystal fabrication process.

We have fabricated five sets of samples with micro-pyramid periods of 110 µm, 70 µm, 60 µm, 45 µm and 30 µm. All samples were examined under a Scanning Electron Microscope (SEM). **Fig. 5.2** shows a SEM image of a silicon photonic crystal with 45-µm-period micro-pyramid surface structure. The facet is very smooth and linear, free of defects visible to the naked eye. In addition, we fabricated AR layers on both the front and back sides of the silicon wafer. This was done by performing step 1 on both sides simultaneously and repeating steps 2-7 on the front and back side of the silicon wafer individually. **Fig. 5.3** shows the SEM image of silicon with 30-µm-period micro-pyramid surface structure on both sides. Excellent pyramidal structures were obtained.
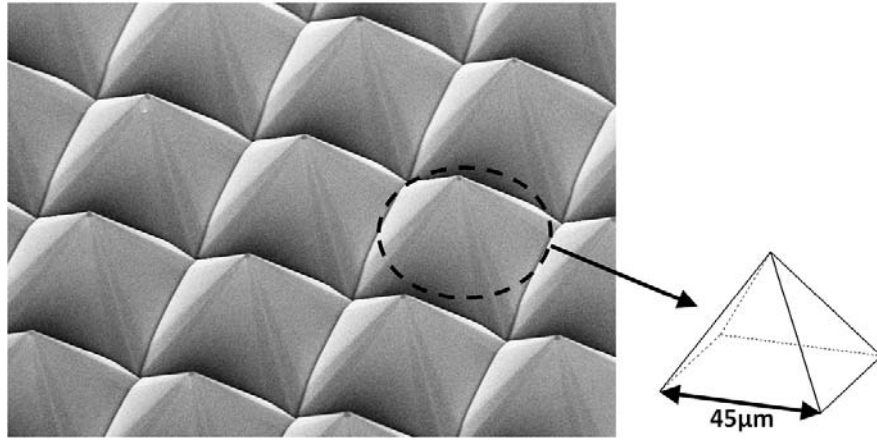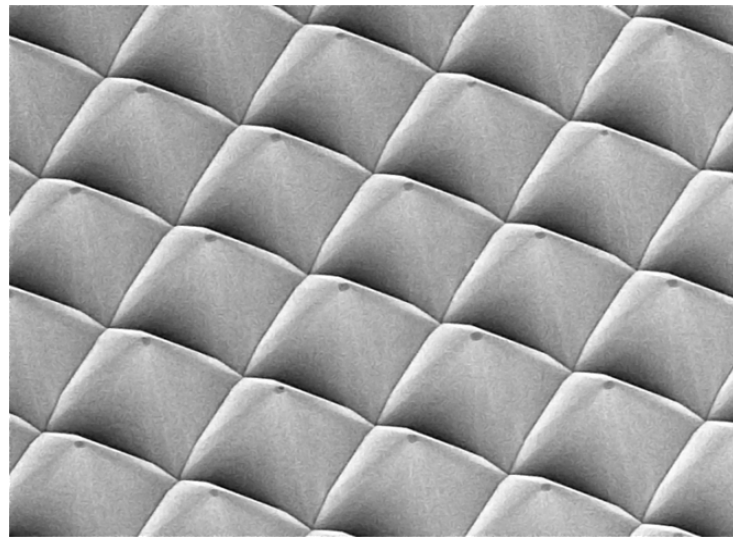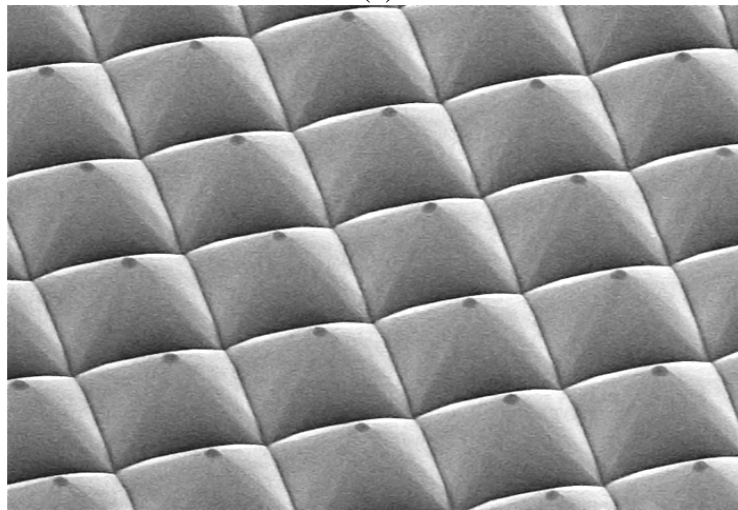
Fig. 5.2 A SEM image of silicon photonic crystal with 45-µm-period micro-pyramid structure on a single side.

(a)

(b)

Fig. 5.3 SEM images of double-sided 30-µm period micro-pyramid structure: (a) front-side, (b) back-side.

5.4   Theoretical Calculation of AR Photonic Crystals

To calculate and simulate the anti-reflection effect of micro-pyramid structures, it is necessary to first determine their effective refractive indexes. In the quasi-static limit, the structure (grating) period is much smaller than the THz wavelength and the dependency of the effective index on the grating period can be neglected. [42] The zero-order effective medium theory (EMT) can be used to obtain the effective index, which gives the following equation in the quasi-static limit ($\Lambda / \lambda \rightarrow 0$):

$$n_{eff} = \sqrt{f \cdot n_2^2 + (1-f) \cdot n_1^2} \qquad (5.1)$$

where Λ is the grating period, λ is the THz wavelength, n_2 (=3.42) is the refractive index of silicon, n_1 (=1) is the refractive index of air and f is the filling factor of silicon at each depth of the photonic structure. To arrive at the filling factor at each depth, the pyramid can be regarded as being composed of an infinite number of layers and the filling factor of each layer is well approximated by the area fraction since the top and bottom surfaces of each layer have virtually the same size. As a result, each depth in these micro-pyramid structures has an effective index of $n_{eff} = \sqrt{f \cdot 3.42^2 + (1-f)}$. [42, 43] When the structure (grating) period is closer to the THz wavelength, a second-order effective medium theory is necessary to describe the effective index, and the expression is given by:

$$n_{eff} = \sqrt{f \cdot n_2^2 + (1-f) \cdot n_1^2 + \frac{\pi^2}{3}(\frac{\Lambda}{\lambda})^2 f^2 (1-f)^2 (n_2^2 - n_1^2)^2} \qquad (5.2)$$

In order to calculate the transmission of electromagnetic waves through these micro-pyramid structures, the matrix theory in optics is applied. Each layer in the micro-pyramid structure is considered as a propagation matrix $P_{(i)}$ in the form of $\begin{bmatrix} e^{-j\varphi_i} & 0 \\ 0 & e^{j\varphi_i} \end{bmatrix}$, where φ_i is the phase shift of each layer. On the other hand, each interface between adjacent layers is considered as a transmission matrix $M_{(i-1)}$ in the form of $\frac{1}{2n_{i+1}} \begin{bmatrix} n_{i+1} + n_i & n_{i+1} - n_i \\ n_{i+1} - n_i & n_{i+1} + n_i \end{bmatrix}$. [44] The overall transmission matrix M is written as:

$$M = P_{(n)} \cdot \prod_{i=n-1}^{1} M_{(i)} P_{(i)} \qquad (5.3)$$

where n is the number of layers, $P_{(n)}$ and $P_{(1)}$ are the propagation matrices for silicon and air, respectively. The transmission and reflection of the system are obtained by converting the transmission matrix M into scattering matrix S.

To simulate THz propagation through the pyramidal photonic crystals, we used the above formulism and set the number of layers to be greater than 500. The convergence of the simulation was confirmed when little difference was observed if the number of layers was over 500. Based on the matrix calculation, the relative transmission amplitude approaches a maximum value of 1.194 at high frequencies for all micro-pyramid structures without considering diffraction. In this case, relative field transmission amplitude of 1.194 is equivalent to zero reflectivity, giving an upper limit on the performance of these AR silicon samples. We note that the AR effect is strongly affected by the height of the pyramid which is directly related with the period of the pyramids by $h = \Lambda/2 \cdot \tan 54.7°$, where Λ is period of the micro-pyramid. For consistency, we discuss AR effect as a function of period throughout this work.

Diffraction effect begins to strongly influence THz transmission in micro-pyramid structures when their periods approach the order of the THz wavelength. As a result, each micro-pyramid structured sample has its specific peak frequency, above which high-order diffraction starts to occur and the transmitted THz amplitude (zero order diffraction) begins to decrease. This frequency is referred to as the cut-off frequency and can be calculated by the following expression at normal incidence:

$$f_c = c/(\Lambda \cdot n) \tag{5.4}$$

where c is the speed of light, Λ is the period of the micro-pyramid and n (=3.42) is the refractive index of silicon in the terahertz range. [45]

In the simulation, we include the diffraction effect by adding an analytical diffraction term $\mathrm{sinc}((f - f_c)/a)$ to the THz transmission function through the micro-pyramid structure, where *a* is a fitting parameter. Therefore, the final overall matrix M' is given by:

$$M' = M \cdot \mathrm{sinc}((f - f_c)/a) \tag{5.5}$$

5.5 Experimental evaluation of AR photonic devices

THz time-domain spectroscopy (THz TDS) in transmission mode was used to evaluate the anti-reflection performance of the silicon photonic crystal samples with various micro-pyramid surface structures. Two different types of THz TDS were employed: traditional TDS using EO sampling and an oscillator laser [46], and TDS using air breakdown coherent detection (ABCD) and an amplifier laser [47].

Fig. 5.4 shows the schematic setup for the THz EO sampling system. A femtosecond oscillator laser was used with a center wavelength at 800 nm, an average power of 900 mW, a pulse width of 80 fs and a repetition rate of 80 MHz. THz radiation was generated from the surface of InAs through the photo-Dember effect. The available spectra of the spectrometer spanned from 0.1 THz to more than 4 THz by using a 200-micron-thick GaP crystal sensor. A planar silicon substrate or samples with AR photonic crystals were positioned in the terahertz beam path with normal incidence and their results were compared. Relative transmission spectra of THz field amplitude were obtained after the THz amplitude spectra through the samples were divided by that through the planar silicon substrate. For THz ABCD spectroscopy, air and amplified pulses were used for both THz generation and detection, which had a broad bandwidth from 0.1 THz to 11 THz.
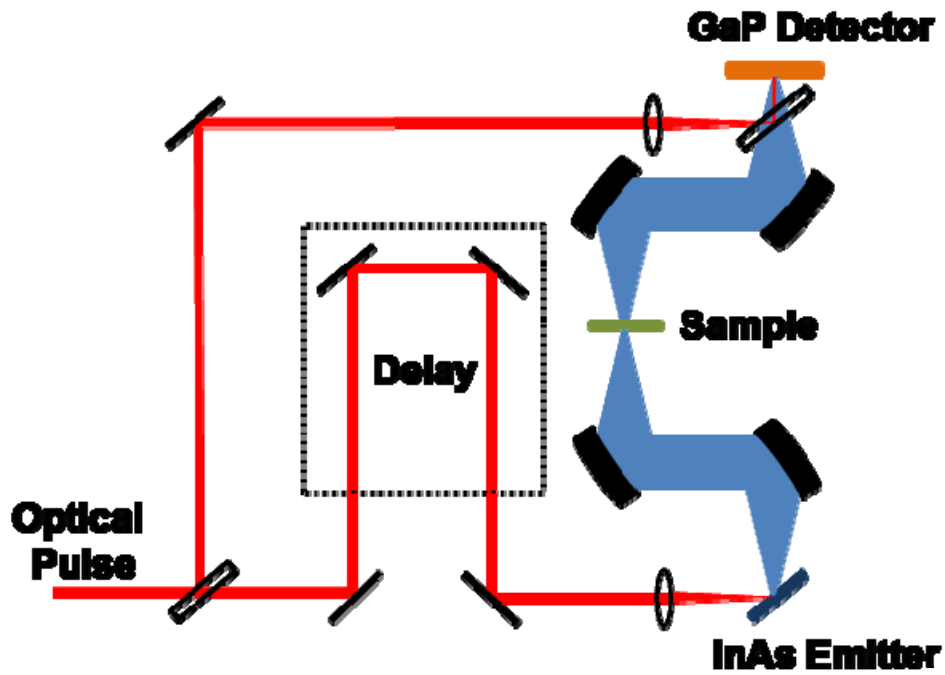

Fig. 5.4 Schematics of THz time-domain spectroscopy setup using EO sampling.

Fig. 5.5 shows the simulated results (solid lines) and experimental results (scattered symbols) of relative transmission with micro-pyramid structures on one side of a silicon wafer which are compared with the planar silicon substrate. The simulated results were obtained by using the transfer-matrix method from 0.2 THz to 10 THz at 0.05 THz steps. The experimental results of each sample were obtained by comparing the Fourier-transformed spectra of the time-domain waveforms. As can be seen from the figure, micro-pyramid structures with periods from 110 µm to 30 µm have relative transmission peak amplitudes of 1.13, 1.12, 1.16, 1.15 and 1.13, respectively. The peaks of relative transmission are located at 0.75 THz, 1.11 THz, 1.41 THz, 1.93 THz and 2.93 THz in the order previously defined. The transmission enhancement effect of these silicon samples has different peak location and bandwidth. Silicon samples with smaller periods have larger anti-reflection bandwidths. Samples with micro-pyramid periods from 110 µm to 30 µm have AR bandwidths of 0.91 THz, 1.35 THz, 1.67 THz, 2.34 THz and 3.15 THz, respectively. [48]
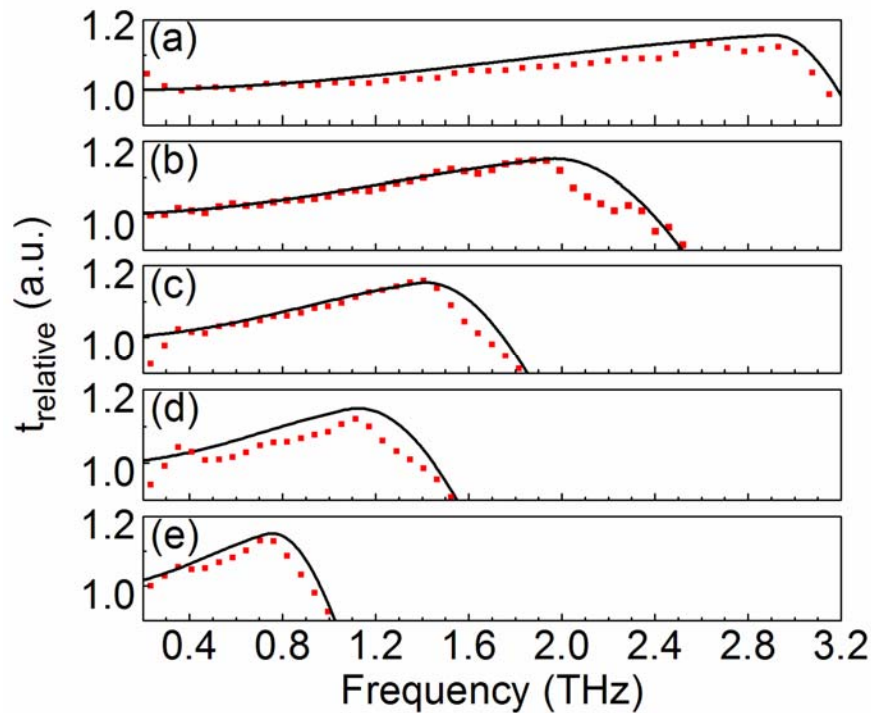

Fig. 5.5 Relative transmission amplitude ($t_{relative}$) of one-sided micro-pyramid structured samples with periods (a) 30 µm, (b) 45 µm, (c) 60 µm, (d) 70 µm and (e) 110 µm. Experimental results are shown by the scattered symbols; simulation results are shown by the solid lines.

The reciprocal of measured cut-off frequency versus micro-pyramid period was plotted in **Fig. 5.6** (a) in scattered symbols. It has a well-defined linear dependence on pyramid structure

period. Experimental results agree well with the calculated ones (represented by the solid line) using the cut-off frequency in equation 5.4. Furthermore, each micro-pyramid structured sample has a particular bandwidth of anti-reflection effect which is also related to the grating structure period. **Fig. 5.6** (b) illustrates the reciprocal of the measured bandwidth against micro-pyramid period in scattered symbols. The experimental results show a linear dependence on pyramid period and are reproduced well by simulation.

To better demonstrate the AR performance of micro-pyramid structured samples, we plot the reflectivity for all the samples. **Fig. 5.7** shows the absolute power reflectivity of each sample, as well as that of planar silicon for comparison. It was obtained by considering reflection and transmission from both surfaces of each sample and using the relative transmission data in **Fig. 5.5**. Samples with different micro-pyramid structure periods show different reduction of reflectivity. Micro-pyramid structures with greater height have better anti-reflection effect in lower frequencies, but it starts to roll off more quickly after its cut-off frequency because of diffraction. For example, the 60-µm-period micro-pyramid structured sample has a minimum reflectivity of 3% at 1.41 THz, corresponding to a maximum reduction of reflectivity by 89%, compared to the planar silicon. However, its anti-reflection effect retrogrades quickly beyond 1.67 THz. The 30-µm-period micro-pyramid structured sample exhibits the best overall anti-reflection effect among all samples and displays superior anti-reflection performance over a broad frequency range. In general the maximum reduction in power reflectivity is over 80% for most samples, compared to the planar silicon.
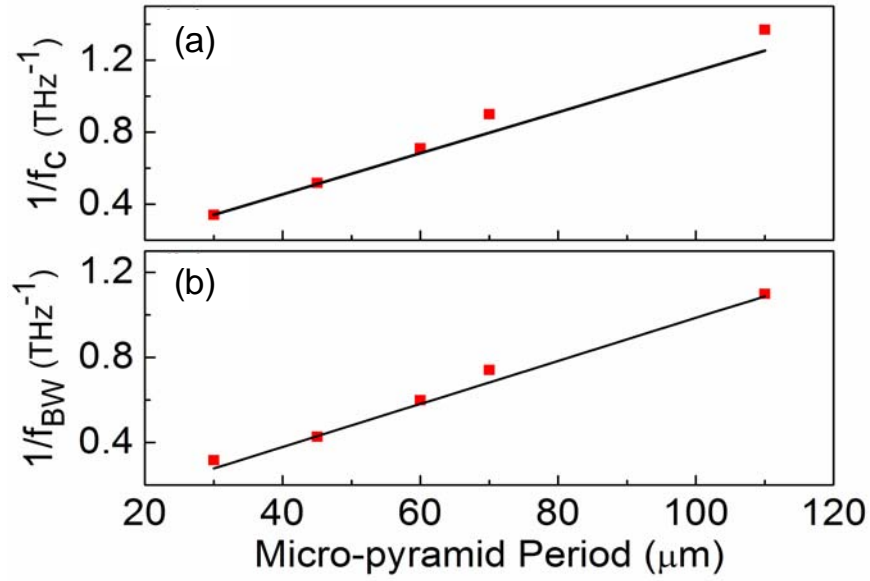
Fig. 5.6 Reciprocals of cut-off frequency (f_C) and bandwidth (f_{BW}) of micro-pyramid structured samples vs. sample periods. Experimental results: scattered symbols; simulation results: solid lines.
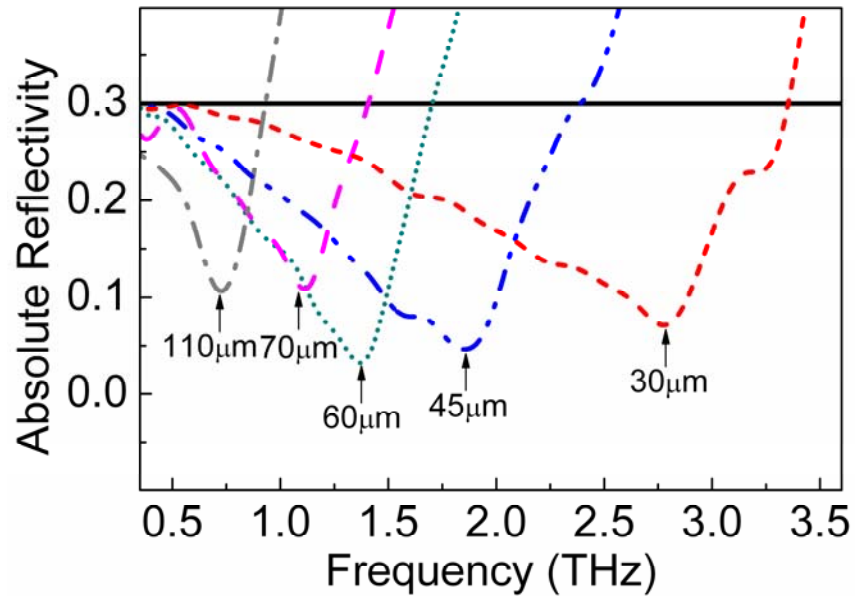

Fig. 5.7 Power reflectivity is plotted for samples with various micro-pyramid structure periods and illustrated by different lines. Reflectivity of planar silicon is shown by the solid line.

5.6   Discussion

Anti-reflection design with crystallographic, wet-etched, micro-pyramid, photonic structure has many unique advantages. The fabricated samples are polarization independent at normal incidence. **Fig. 5.8** (a) shows the azimuthal angle-dependence of the transmitted THz power amplitude of the 60-µm period sample. The amplitude virtually stayed the same as the azimuthal angle was rotated from 0 to 360 degrees. Besides, the samples are mostly independent of incident angle when the angle is less than 20 degrees, as shown in **Fig. 5.8** (b), which illustrates transmitted THz power as a function of incident angle for the sample with a 60-µm period

Furthermore, the size of the pyramid can be precisely controlled to tune the bandwidth and cut-off frequency. This method is relatively easy to use and has a short fabrication cycle. Mass production is readily available because conventional lithography and etching techniques of the semiconductor industry are used. In addition, the size of the pyramid is in the order of tens of microns and does not alter the silicon substrate too much. Optimization of the pyramid profile may result in broader spectra of enhanced transmission. Although the devices have been demonstrated as anti-reflection devices on the silicon substrate, this design can be also used for other substrate materials, such as semiconductors, polymers, and so on.

It is worthwhile to point out that these silicon-based photonic crystals also act as a low-pass filter. A broadband THz transmission spectrum through a silicon device with 30-µm period photonic crystal structures on both sides is shown in **Fig. 5.9**. It functions as a low-pass filter, where THz components with frequency below 3 THz can pass through and are enhanced. When THz components are above 3 THz, their amplitudes quickly decrease to the noise floor. Double-sided AR devices have a sharper transition edge as a filter than single-sided AR devices, in addition to the higher transmission. Since the bandwidth of AR photonic crystals can be tuned, this technique provides a way of fabricating a tunable bandpass filter for THz waves.
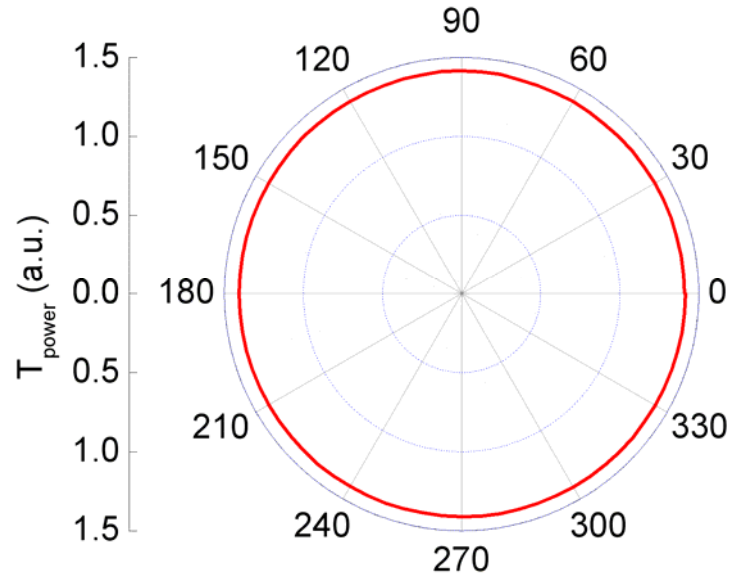
(a)
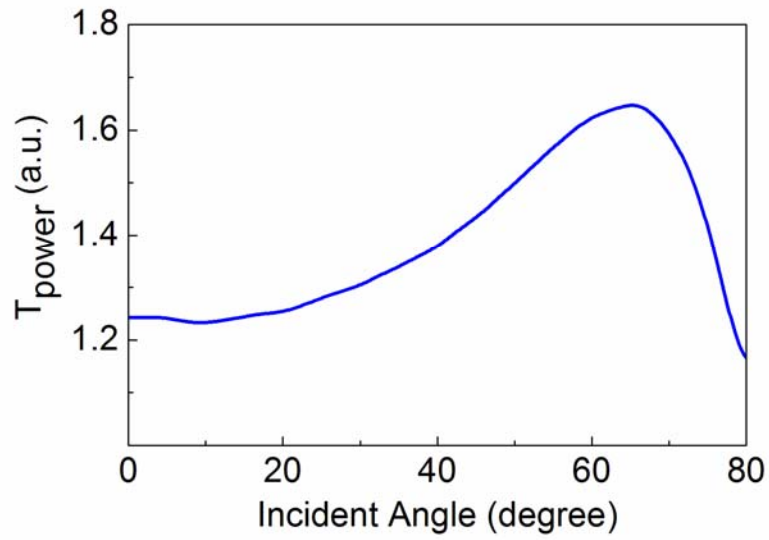
(b)

Fig. 5.8(a) Transmitted THz power versus azimuthal angle; (b) Transmitted THz power versus incident angle. Both measurements are performed on the photonic sample with 60 µm period.
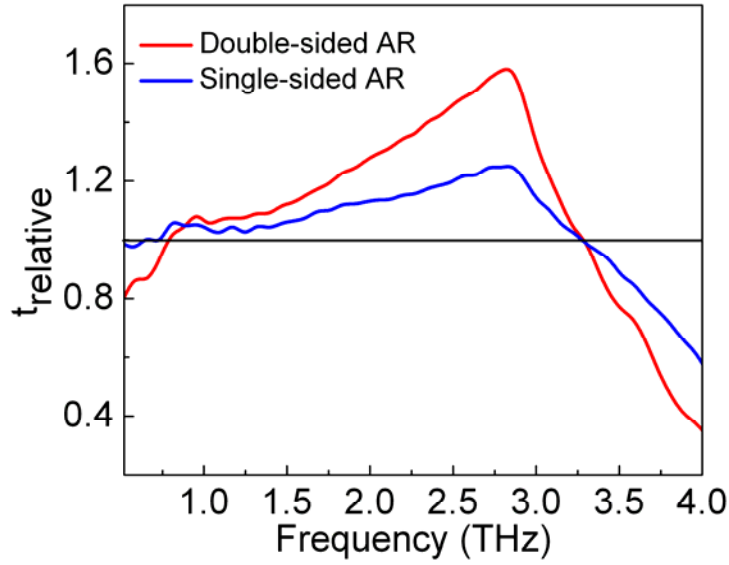
Fig. 5.9 Relative transmission amplitude ($t_{relative}$) of two-sided and single-sided micro-pyramid structured samples with 30-µm period. The two-sided sample exhibits low-pass filter effect.

6.   Multi-layer Photonic Devices

6.1   Background

Anti-reflection techniques in the visible wavelengths are well developed, whereas in the terahertz range research is still underway to look for the right materials and implementation. High resistivity silicon is a suitable material for a wide range of terahertz (THz) components such as windows, filters and beam splitters because of its high transparency and low dispersion in the whole THz range; however, it is associated with high Fresnel loss due to high index of refraction. To alleviate the high loss and reduce interference, anti-reflection (AR) techniques have recently attracted a lot of attention. AR of electromagnetic waves can be realized using several methods, including single-layer interference design [30, 31], absorptive AR design, inhomogeneous design [28, 29, 35-37, 48-51] and multi-layer design [33, 34]. For application in THz time-domain spectroscopy, absorptive AR devices cannot be used because transmission through THz components is usually necessary. Single-layer design is the most straight-forward way to realize anti-reflection effect with the downfall of a narrow bandwidth. For both single-layer and multi-layer design, suitable materials with the right index properties such as AR films are nearly impossible to find naturally. [30, 31, 33] To find a solution, researchers have attempted to alter the refractive index of materials using a modified structure. For example,

silicon nano-tips [35], thin metal layers [49-51], and surface relieve structures [28, 29, 36, 37, 48] have been employed as THz AR devices. Most of these explorations utilize a single-layer design, which is associated with either limited AR bandwidth [28, 29, 35-37, 48] or significant insertion loss [49-51].

6.2 Technical approach

In this work, we propose to achieve the desired refractive index and thickness by selectively etching off part of the silicon with specific patterns. The fabricated device has a three-layer structure. In each layer, a certain percent of silicon is removed in the form of rectangular columns, resulting in a 2-dimensional grating with air columns as the periodic elements. The final product is a three-dimensional photonic grating device, with each layer having its own air/silicon volume ratio and thickness. The fabricated device has premium anti-reflection performance throughout almost the entire THz band and its performance does not significantly depend on polarization or incident angle. Moreover, the concept can be used for most semiconductors and at other wavelengths.

The concept of this multi-layer device is based on gradient-index, anti-reflection coating theory [52]. A continuous Gaussian profile is first calculated with maximum (silicon) and minimum (air) refractive indices. Then a discretization procedure is applied to obtain the refractive indices of multiple laminar layers and their corresponding thickness per unit wavelength (i.e. the wavelength of the propagating optical beam). Anti-reflection performance is better with more laminar layers. In our research, we choose a three-layer design due to fabrication feasibility and its satisfying anti-reflection effect. The total thickness of the three-layer device is comparable to unit wavelength. In addition, center frequency of the device's anti-reflection profile will be dependent of the total thickness. The anti-reflection profile will center at low frequency for a device with large structure thickness and at high frequency for small structure thickness. Therefore, by choosing different structure thickness the anti-reflection profile can be tuned accordingly. Using transfer matrix method, the normal incidence reflectance of this three-layer device can be calculated. Each layer can be represented by a propagation matrix,

$$P_{(i)} = \begin{bmatrix} e^{-j\varphi_i} & 0 \\ 0 & e^{j\varphi_i} \end{bmatrix} \qquad (6.1)$$
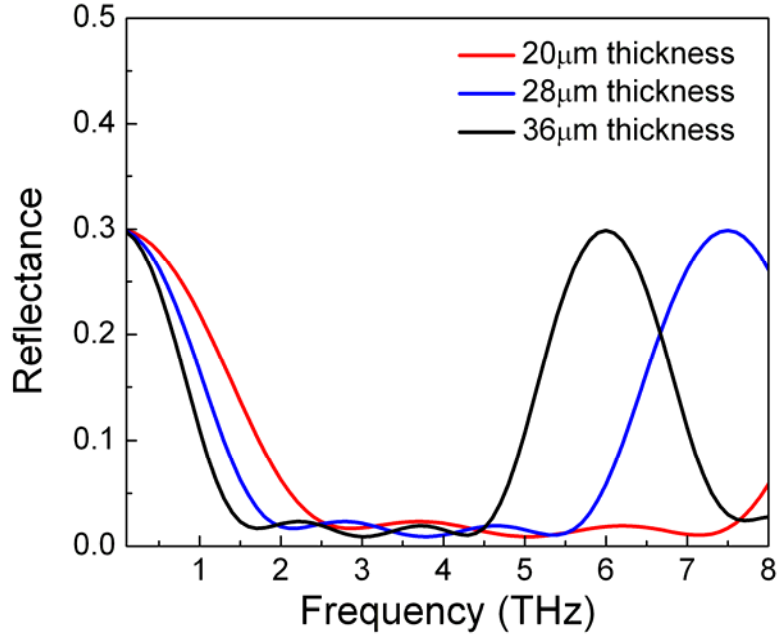
Fig. 6.1 Simulated reflectance spectra of three-layer, anti-reflection, photonic gratings with total thickness of 20 µm, 28 µm and 36 µm, plotted in red, blue, and black curves respectively. The shallower device has a better performance at high frequency while the deeper device has lower reflectance at low frequency (< 2.5 THz).

where φ_i is the corresponding phase shift of each layer. Each interface between two adjacent layers can be represented by a transmission matrix,

$$T_{(i)} = \frac{1}{2 \cdot n_{i+1}} \begin{bmatrix} n_{i+1} + n_i & n_{i+1} - n_i \\ n_{i+1} - n_i & n_{i+1} + n_i \end{bmatrix} \tag{6.2}$$

where n_i and n_{i+1} are the refractive indices of two neighboring layers. Therefore, the transmission matrix representing a three-layer device in between air and silicon can be written as:

$$M = P_{(0)} \prod_{i=1}^{4} T_{(i-1)} P_{(i)} \tag{6.3}$$

where $P_{(0)}$ and $P_{(4)}$ are the propagation matrix of air and silicon, respectively. By converting transmission matrix M into scattering matrix S, reflectance and transmittance can be readily acquired. **Fig. 6.1** shows the reflectance of a three-layer, inverted, photonic grating device with total thickness of 20 µm, 28 µm and 36 µm. The center AR frequency and bandwidth clearly depends on the total thickness of the structure. In our experiments, the effective refractive indices of each layer are realized by etching air columns of different density in silicon and tuning the air-to-silicon ratio. In regular gratings, silicon would be the material of the periodic elements.

However, the air ratio is very low for the layer that is closest to bulk silicon. If silicon is used as periodic elements, the opening between elements will be too narrow for effective ion etching. Therefore, we use air columns as the periodic elements and silicon as the spacing between elements, so that both the air column and the silicon spacing have reasonable size to facilitate etching. We call this new design inverted photonic grating.

6.3 Device fabrication

Applying the capacitor-like formula to the air column structure [53], the effective refractive index of each layer can be derived as:

$$n = \sqrt{\frac{n_{silicon}^2 \cdot a}{n_{silicon}^2 \cdot a + 1 - a} + n_{silicon}^2 \cdot (1-a)} \tag{6.4}$$

where a is the square root of the filling factor of air columns in a specific layer. In the design of the AR devices, two parameters are especially important: device thickness that is related with center AR frequency and structure period that is related with diffraction. Considering diffraction occurs when the period of the structure approaches the order of terahertz wavelengths, broadband AR can only be achieved when the structure period is small enough. For example, in our devices, the period is set to 20 µm or 15 µm, which roughly correspond to diffraction limits of 6 THz or 8 THz, respectively. On the other hand, to achieve anti-reflection throughout most of the THz band, a device thickness of 20 µm is chosen for the design such that the achievable reflectance of the device can go below 5% from 2 THz to over 6 THz. The design parameters of this three-layer device are shown in **Table 6.1**.

Fabrication of the three-layer, inverted, photonic grating device starts with standard UV-lithography, which is employed to define the photo-resist hard mask. The photo-resist hard mask will act as a protection layer during the subsequent etching process. Deep reactive ion etching (DRIE) is used to etch the silicon in order to achieve a high aspect ratio in the three-layer device. Photo-lithography and etching processes start with the deepest layer in the silicon and are repeated two times from the bottom up to fabricate the entire device. Furthermore, all layers are aligned using a marker during fabrication to make sure that the air columns are in the right positions. Schematic of the inverted photonic grating device is illustrated in **Fig. 6.2(a)**; **Fig. 6.2(b)** and **6.2(c)** show scanning electron microscope (SEM) images of the fabricated devices in

the top view and cross-section view. The three layers of the device are aligned at the lower left corners.

Layer	Air	1	2	3	Silicon
Refractive Index	1	1.55	2.25	2.95	3.42
Layer Height		8.9 µm	6.3 µm	4.8 µm	
Air ratio (%)	100	77.44	42.25	10.89	0
Hole Dimension (Λ=20 µm)		17.6 µm × 17.6 µm	13.0 µm × 13.0 µm	6.6 µm × 6.6 µm	
Hole Dimension (Λ=15 µm)		13.2 µm × 13.2 µm	9.7 µm × 9.7 µm	4.9 µm × 4.9 µm	

Table 6.1 Design parameters of three-layer, inverted, photonic gratings with periods of 20 µm and 15 µm.
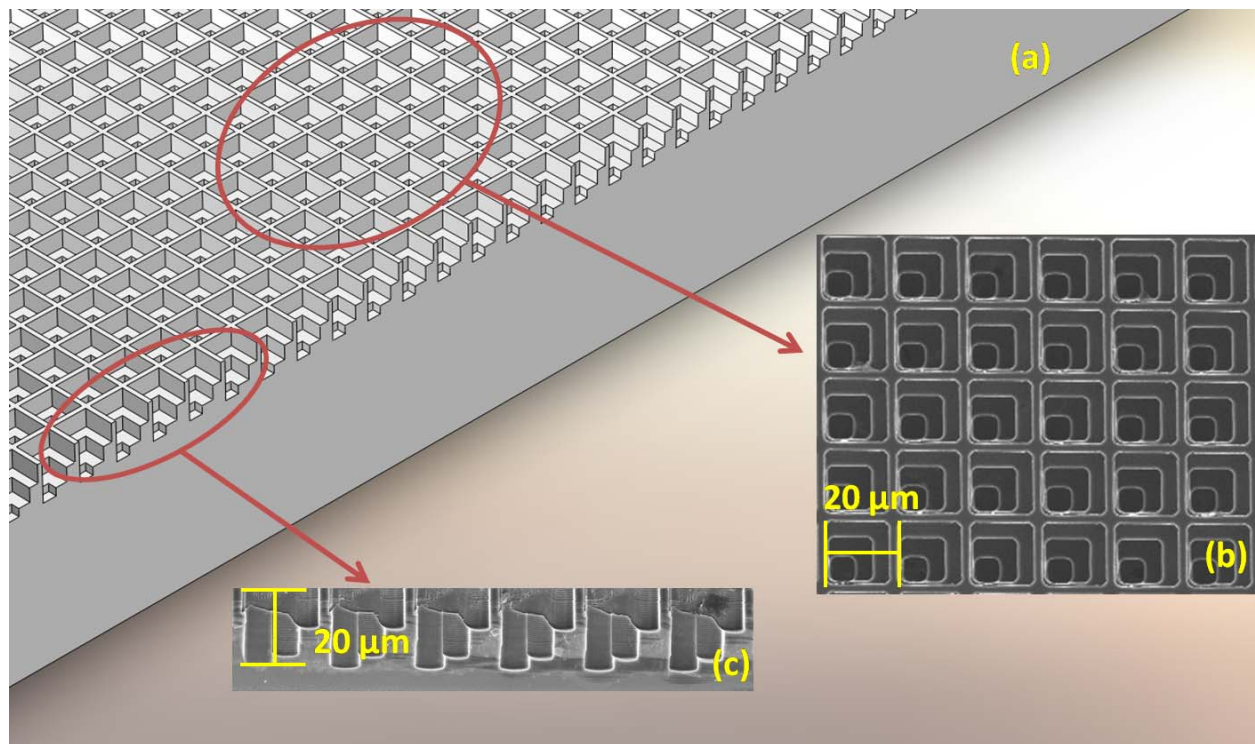

Fig. 6.2 Schematic (a) and scanning electron microscope images of a 20-µm thick device with 20-µm structure period in top view (b) and cross-section view (c). The device has three layers of air columns etched into a silicon substrate, which form the inverted photonic gratings.

6.4   Device evaluation

A terahertz air-biased-coherence-detection (THz-ABCD) system [47, 54] is employed for evaluation of the fabricated 20-µm-thick AR devices. The system has a bandwidth from 0.2 THz to over 10 THz. A planar high resistivity silicon wafer is designated as the reference. Since high resistivity silicon has very little absorption in the terahertz range, the incident wave will be reflected, transmitted or diffracted at the AR device interface, as illustrated in **Fig. 6.3**.
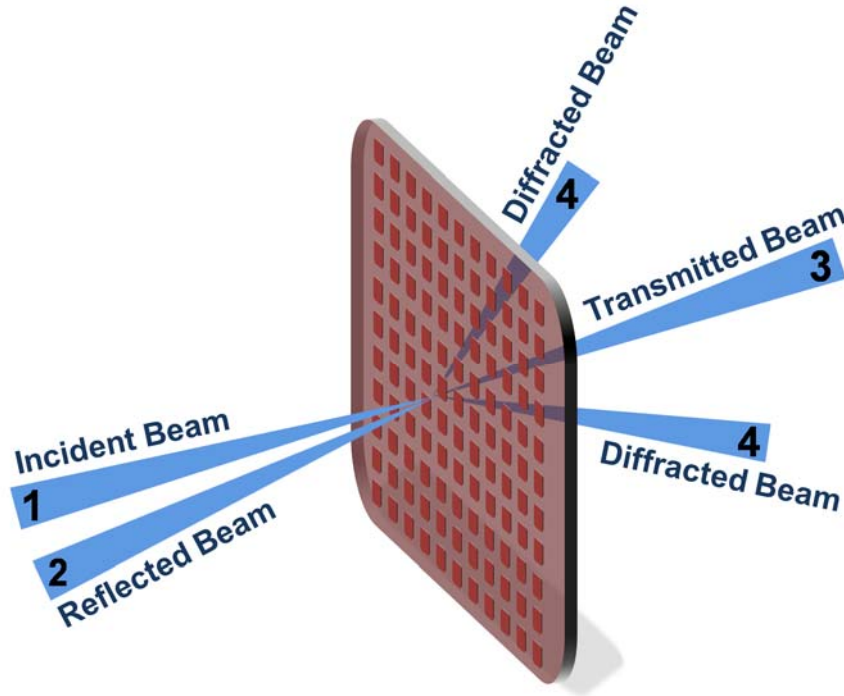

Fig. 6.3 Illustration of optical beams at the AR interface: incident beam (1), reflected beam (2), transmitted beam (3) and diffracted beams (4).

First, we study the reflectance of the inverted photonic grating devices. **Fig. 6.4(a)** shows the reflected THz time-domain waveforms from the silicon reference, an AR device with 20-µm period structures and an AR device with 15-µm period structures. The reflected waveform amplitudes of the AR devices are much smaller than the silicon reference, showing significant anti-reflection effect. In order to quantify the frequency-dependent, anti-reflection performance we calculate the power reflectance from the Fourier-transform spectra, which is shown in **Fig. 6.4(b)**. The reflectance of the 20-µm period device and the 15-µm period device are plotted in

blue curve and red curve respectively. Reflectance of the devices is reduced to less than 5% from 2.2 THz to 5.5 THz.

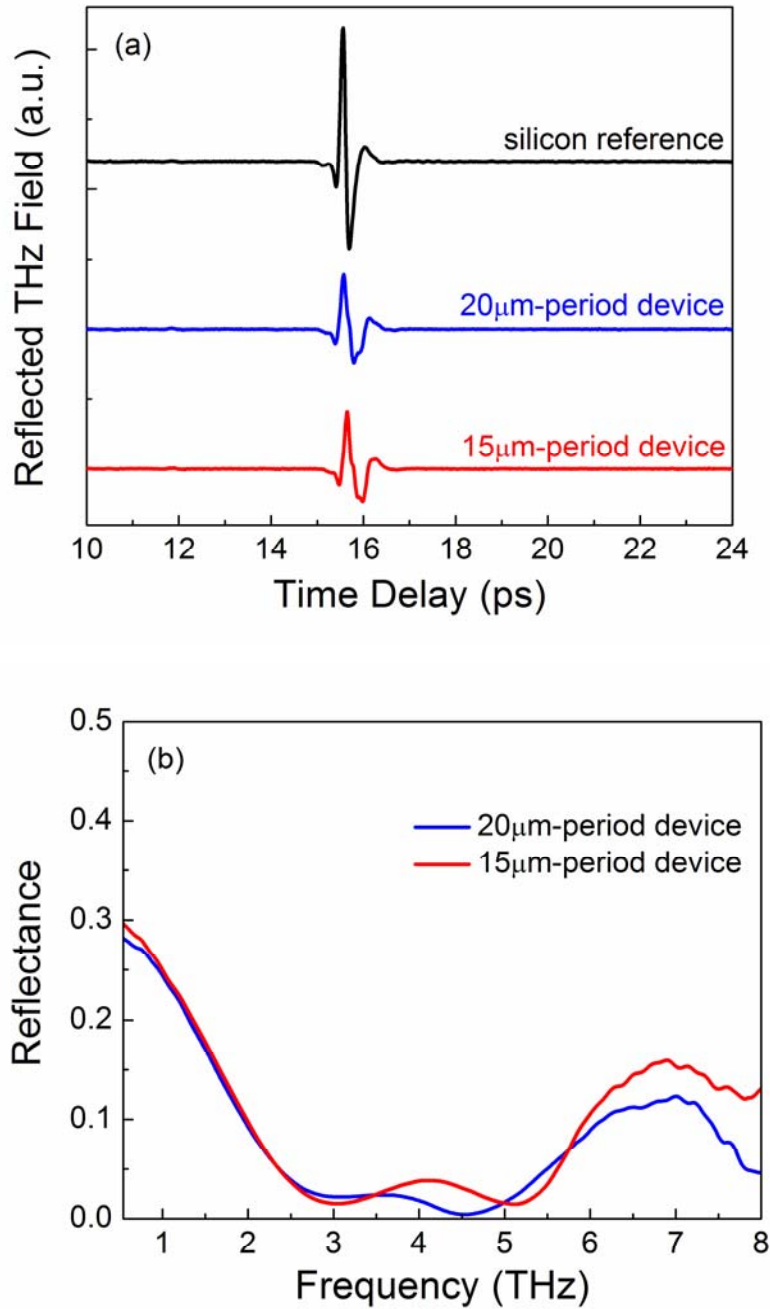**Fig. 6.4** (a) Reflected THz time-domain waveforms of silicon reference (black curve), 20-µm period anti-reflection device (blue curve) and 15-µm period anti-reflection device (red curve). Waveforms of both anti-reflection devices show substantially smaller amplitudes than that of the silicon reference. (b) Reflectance spectra of 20-µm period anti-reflection device (blue curve) and 15-µm period anti-reflection device (red curve).

In order to investigate whether reduction in reflectivity leads to enhanced transmission, we measure the THz waveform in the transmission direction (i.e. 0th order diffraction) and analyze the experimental results to understand both transmission and diffraction of the inverted photonic gratings. The transmitted time-domain waveforms of the silicon reference, the 20-µm period device and the 15-µm period device are shown in **Fig. 6.5(a)**. Enhanced transmission can be observed from the increased peak-to-peak amplitudes of the 20-µm period and 15-µm period devices. For better comparison of frequency-dependent AR performance, relative transmission spectra of the two devices are plotted as solid lines in **Fig. 6.5(b)**. They are derived from the Fourier-transform spectra of the waveforms and normalized to that of the silicon reference. Also in **Fig. 6.5(b)**, simulation results of the 20-µm period and 15-µm period devices are plotted in dotted lines. Theoretically, relative field transmission can be calculated by [44]

$$t_{relative} = \sqrt{\frac{1 - R_{structures}}{1 - R_{silicon}}} \quad (6.5)$$

where

$$R_{silicon} = \left(\frac{n_{silicon} - n_{air}}{n_{silicon} + n_{air}} \right)^2 \quad (6.6)$$

For a perfect AR device (0% reflectance) of silicon at THz frequency, the relative field transmission is 1.1947, which is the upper limit. The experimental results fit nicely with the simulation result before diffraction occurs. When the THz wavelength approaches the order of the devices' structure periods, diffraction takes place at

$$\lambda = \Lambda \cdot n_{silicon} \quad (6.7)$$

where λ is the THz wavelength and Λ is the structure period [45]. This causes the decline in transmission as seen in **Fig. 6.5(b)**. For the 20-µm period device, diffraction starts at around 4.3 THz; in the 15-µm period device, diffraction starts roughly at 5.8 THz. As frequency increases above the diffraction threshold, diffraction dominates over transmission; consequently anti-reflection effect ceases at 5.9 THz for the 20-µm period device and 7.3 THz for the 15-µm period device. The observed diffraction effect is in good agreement with theoretical calculation using Equation 7, where the diffraction threshold is calculated to be 5.7 THz for the 20-µm period device and 7.1 THz for the 15-µm period device. Furthermore, the 3dB bandwidth of the device spans from 1.4 THz to 6 THz, which defines center frequency -- $(f_L+f_H)/2$ at 3.7 THz. Thus, the relative 3dB bandwidth, which can be defined as $\delta f/f_c$, is as large as 116.2%.
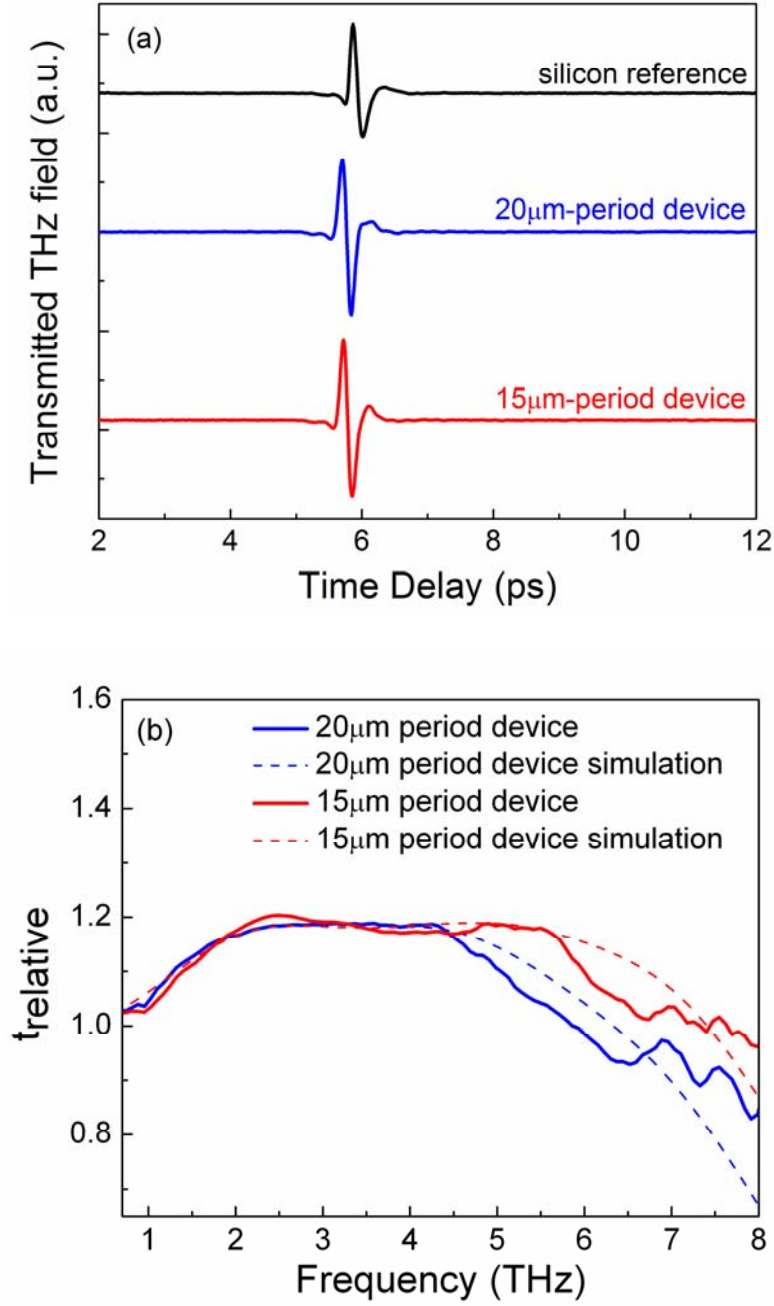
Fig. 6.5 (a) Transmitted THz time-domain waveforms through silicon reference (black curve), 20-µm period three-layer anti-reflection device (blue curve) and 15-µm period three-layer anti-reflection device (red curve). Considerable transmission enhancement is observed from the waveform amplitudes of the two devices as compared to the silicon reference. (b) THz relative transmission spectra of 20-µm period three-layer anti-reflection device (blue curve), 15-µm period three-layer anti-reflection device (red curve) and simulated results (corresponding dotted lines). As diffraction starts to dominate over direct transmission, anti-reflection performance diminishes at higher frequencies.

Fig. 6.6 (a) Relative transmission at center frequency (3.7 THz) of the 15 µm period device is plotted against the azimuthal angle as it increases from 0 degrees to 180 degrees in 22.5 degree steps. Throughout the 180 degree range, relative transmission amplitude abides at the same level, showing no dependence on polarization. (b) Relative transmission at center frequency of the 15 µm period device is plotted against incident angle from 0 degrees to 50 degrees in 10 degree steps. For incident angle less than 30 degrees, relative transmission remains within 2% compared with normal incidence. As incident angle further increases, anti-reflection performance noticeably deteriorates.

For an AR device to be practical and useful, it is desirable for its function to be independent of polarization and incident angle. To further evaluate the inverted photonic grating as an AR device, we study its polarization dependence and incident angle dependence. **Fig. 6.6(a)** shows the measure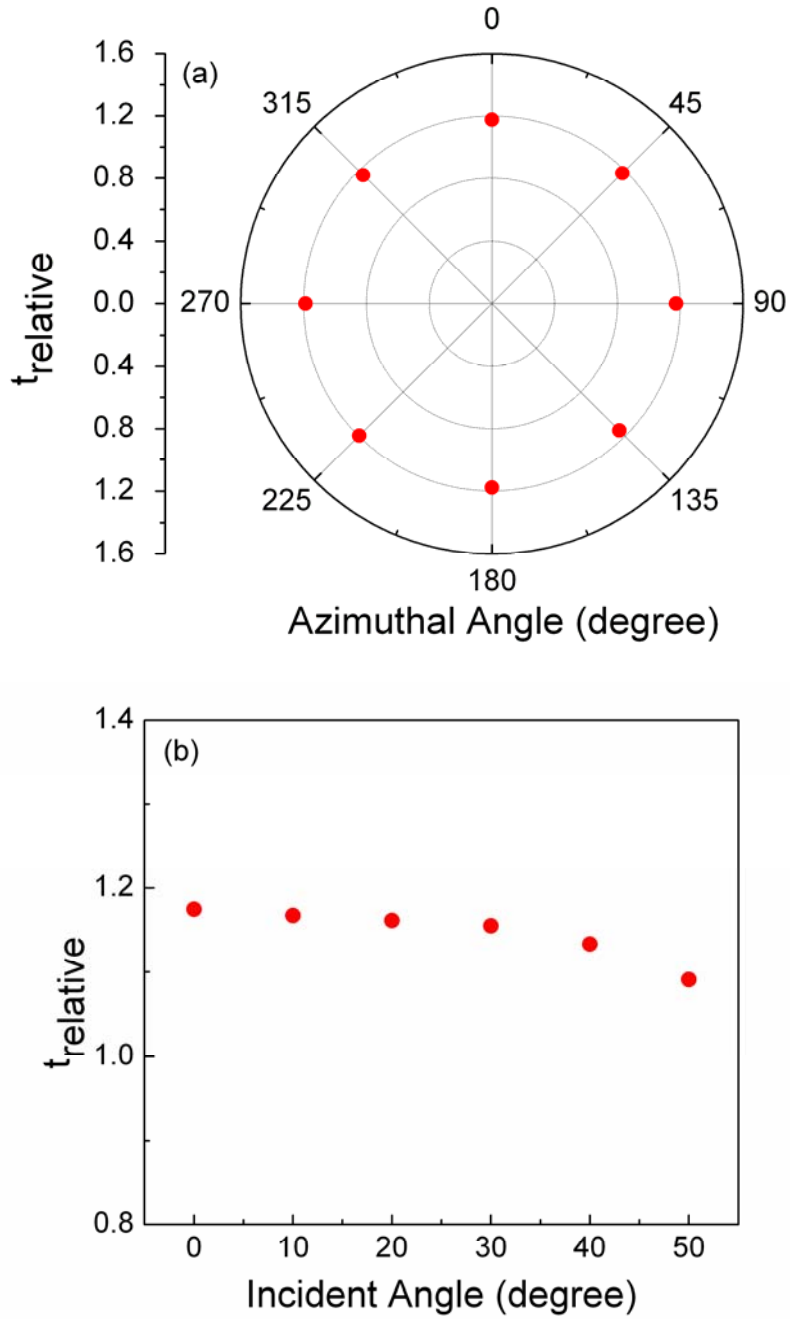d relative transmission at center frequency (3.7 THz) of the 15-µm period device as the azimuthal angle increases from 0 degrees to 180 degrees in 22.5 degree steps. As seen from the result, relative transmission amplitude changes less than 2% as the azimuthal angle changes from 0 degrees to 180 degrees, which indicates that the anti-reflection performance of the devices is independent of polarization. On the other hand, anti-reflection performance of the 15-µm period with various incident angles is shown by the relative transmission at center frequency in **Fig. 6.6(b)**. For incident angle less than 30 degrees, relative transmission only decreases 1.7% compared to normal incidence. However, as the incident angle further increases, anti-reflection effect drastically declines.

6.5   Discussion

This three-dimensional, multi-layer, inverted, photonic grating design has several unique qualities. Firstly, this technique allows precise control. By changing the air/silicon volume ratio, the effective refractive index of each layer can be engineered to be any value between 1 and 3.42. Multi-layer design can be readily implemented with each layer having the ideal parameters. Secondly, the method has great flexibility and tunability. The desired working frequency and bandwidth can be achieved by tuning the layer thickness and effective refractive index. Thirdly, the fabricated samples are easy to use because they are polarization-independent at normal incidence and are mostly independent of incident angle below 30°. Fourthly, the etching depth of the device is of the order of tens of microns and does not alter the silicon substrate too much. Fifthly, the fabrication methods involved are standard semiconductor-processing procedures, which result in low-cost production, high throughput, great reliability, and can be applied to other materials at any wavelength. For example, for application as AR devices at mid-infrared wavelengths, an air column with diameter and height around 500 nm is required. Finally, technology involving silicon-based micro-fabrication is very mature, allowing system integration with other functions, such as waveguide, emitter and receiver.

In conclusion, we have designed, fabricated, and evaluated a three-dimensional, inverted, photonic grating device that reduces reflectance from 0.2 THz to 7.35 THz and has a 3dB anti-reflection bandwidth of 4.7 THz with structure period of 15 µm. Through selective etching with

a designed pattern, the desired index and thickness profile can be precisely obtained for optimum performance. As a result, the center AR frequency can be controlled by fabricating devices with different thickness so as to accommodate the applications at different frequency bands. Anti-reflection performance of the fabricated devices is independent of polarization and incident angle to a large extent. The total thickness of the devices (20 µm) is much smaller than THz wavelength, making it compact and compatible with a wide range of terahertz systems. Finally, the fabrication methods involved are standard semiconductor-processing procedures and can be applied to other materials at any wavelength

7.   Achieved Milestones

7.1   THz emission microscope

- A novel THz emission microscope has been constructed and demonstrated with ultra-high spatial resolution.

- A detailed model has been established to explain experimental results and to have a clear understanding of the mechanism of the system.

- 1-nm lateral spatial resolution has been demonstrated experimentally; spectral range of the system extends from 0.1 to 2 THz.

- An isolation platform has been built to host the THz microscope.

- A 2-D imaging system has been constructed with a step resolution of 0.2 nm.

- Spectroscopic imaging of a variety of nano-scale objects have been successfully obtained, including hetero-structure interface, nano quantum dots, minute metallic gratings and nano size GaAs wells.

7.2   THz near-field microscope

- A new near-field microscope apparatus comprised of tapered waveguides has been designed and fabricated using typical semiconductor industry technology.

- THz field propagation and distribution through the tapered waveguides has been simulated using SEM software.

- Quasi-adiabatic process in the tapered waveguides has been demonstrated using various samples in the form of power enhancement and sub d^6 dependence on the aperture diameter.

7.3   THz photonic devices

- Silicon devices with micro-pyramid, photonic crystal structure have been fabricated by crystallographic wet-etching, which resemble the moth-eye structures.

- Silicon photonic devices have demonstrated tunable and broadband anti-reflection performance: Anti-reflection effect is achieved in the broad frequency range of 0.2 THz to 3.15 THz and a maximum 89% reduction in reflectivity of THz power is observed when the sample with 60-µm-period micro-pyramids is used, compared with the reflectivity of a planar silicon substrate.

- The cut-off frequency of enhanced transmission is tuned from 0.74 THz to 2.93 THz and the bandwidth of enhancement increases from 0.91 THz to 3.15 THz, respectively by varying the period of the micro-pyramid photonic devices from 110 µm to 30 µm.

- The silicon photonic crystals function as useful THz components, such as low-pass filters.

7.4   Multi-layer photonic devices

- Three-dimensional, multi-layer, inverted, photonic grating devices have been designed, fabricated and evaluated by DRIE.

- Silicon photonic devices has demonstrated tunable and broadband anti-reflection performance: Anti-reflection effect is achieved in the broad frequency range of 0.2 THz to 37.35 THz and a maximum 90% reduction in reflectivity of THz power, compared with the reflectivity of a planar silicon substrate.

- A 3dB anti-reflection bandwidth of 4.7 THz is achieved in the device with a structure period of 15 µm.

- Anti-reflection performance of the fabricated devices is independent of polarization and incident angle to a large extent.

- The total thickness of the devices (20 µm) is much smaller than THz wavelength, making it compact and compatible with a wide range of terahertz systems.

- The fabrication methods involved are standard semiconductor-processing procedures and can be applied to other materials at any wavelength.

8. Accomplishments

8.1 Journal publications:

- Y. T. Chen, P. Y. Han, and X.-C. Zhang, "Tunable broadband antireflection structures for silicon at terahertz frequency", *Applied Physics Letters*, 94, 041106 (2009).

- Research Highlights, "terahertz trials: the Great pyramids of silicon", *Nature Photonics*, 3, 187, April (2009)

- P. Y. Han, Y. T. Chen, and X.-C. Zhang, "Application of Silicon Micro-pyramid Structures for Anti-reflection of Terahertz Waves", IEEE J. Sel. Topic Quant. Electro., DOI 10.1109/JSTQE.2009.2031164 (2010).

- J. Chen, P. Y. Han, and X.-C. Zhang, "Terahertz-field-induced second-harmonic generation in a beta barium borate crystal and its application in terahertz detection", Appl. Phys. Lett. V. 95, 011118 (2009).

- P. Y. Han, W. Liu, Y.-H Xie and X.-C. Zhang, "Graphene and terahertz science", Wuli, V. 38, No. 6, p. 395-400 (2009).

- Y. T. Chen, P. Y. Han, and X.-C. Zhang, "How to design and build ultra-broadband anti-reflection layer on silicon in THz range", S*ubmitted to Nature Photonics*, (2010).

8.2 Conference Publications:

- P. Y. Han, J. Chen, H. W. Zhao, B. Schulkin, Y. Q. Chen, G. Bastiaans, J. Warrender, and X.-C. Zhang, "Application of terahertz spectroscopy in security, chemistry and microscopy", *invited paper in laser applications to chemical, security and environmental analysis topical meeting* (2008).

- Pengyu Han, Yuting W. Chen, and X.-C. Zhang, "Application of Silicon Photonic devices as an Anti-reflection Layer for Terahertz Waves", *Nanoelectronic Devices for Defense & Security Conference* (2009).

●   Yuting W. Chen, "Application of Silicon Photonic Crystals for Anti-reflection of Terahertz Waves", *IGERT Annual Meeting* (2009).

8.3   Patent filed:

●   X.-C. Zhang, P. Y. Han, Y. T. Chen, "Tunable Broadband Anti-Reflection Apparatus for Silicon at Terahertz Frequency".

8.4   Student Degree Awarded:

●   Yuting. W. Chen, Master of Science, 2009.

9.   Reference:

1. Ferguson, B., Zhang, X.-C. *Materials for terahertz science and technology*, *Nature Materials* **1**, 26 - 33 (01 Sep 2002).

2. Zandonella, C. *Terahertz imaging: T-ray specs*, *Nature* **424**, 721 - 722 (14 Aug 2003).

3. Cole, B. E., Williams, J. B., King, B. T., Sherwin, M. S., Stanley, C. R. *Coherent manipulation of semiconductor quantum bits with terahertz radiation*, *Nature* **410**, 60 - 63 (01 Mar 2001).

4. Huber, R., Tauser, F., Brodschelm, A., Bichler, M., Abstreiter, G., Leitenstorfer, A. *How many-particle interactions develop after ultrafast excitation of an electron-hole plasma*, *Nature* **414**, 286 - 289 (15 Nov 2001).

5. Carr, G. L. *et al. High-power terahertz radiation from relativistic electrons*, *Nature* **420**, 153 - 156 (14 Nov 2002).

6. Köhler, R. *et al. Terahertz semiconductor-heterostructure laser*, *Nature* **417**, 156 - 159 (09 May 2002).

7. R. A. Kaindl, M. A. Carnahan, D. Hägele, R. Lövenich, D. S. Chemla, *Ultrafast terahertz probes of transient conducting and insulating phases in an electron-hole gas*, *Nature* **423**, 734 - 738 (12 Jun 2003).

8. Wang, K., Mittleman, D.M. *Metal wires for terahertz wave guiding*, *Nature* **432**, 376 - 379 (18 Nov 2004).

9. Specht, M., Pedarnig, J.D., Heckl, W.M., Ha¨nsch, T.W. *Scanning Plasmon Near-Field Microscope*, *Phys. Rev. Lett*., **68**, 476–479 (1992).

10. Zenhausern, F., Martin, Y., Wickramasinghe, H.K. *Scanning interferometric apertureless microscopy: Optical imaging at 10 angstrom resolution*, *Science* **269**, 1083–1085 (1995).

11. Knoll, B., Keilmann, F. *Near-field probing of vibrational absorption for chemical microscopy, Nature* **399**, 134–137 (1999).

12. Hillenbrand, R., Keilmann, F. *Material-specific mapping of metal/ semiconductor/dielectric nanosystems at 10 nm resolution by backscattering near-field optical microscopy, Appl. Phys. Lett.* **80**, 25–27 (2002).

13. Valk, N. van der, Planken, P. *Electro-optic detection of subwavelength terahertz spot size in the near field of a metal tip*, *Appl. Phys. Lett.,* **81**, 1558-1560 (2002).

14. Wang, K. L., Barkan, A., Mittleman, D. M. *Sub-wavelength resolution using apertureless terahertz near-field microscopy, Conference on Lasers and Electro-Optics (CLEO) (IEEE Cat. No. CH37419-TBR)*, 2 (2003).

15. Chen, H.-T., Kersting, R., Cho, G.C. *Terahertz imaging with nanometer resolution, Appl. Phys. Lett.* 83, 3009-3011 (2003).

16. Wu, Q., Litz, M., Zhang, X.-C. *Broadband detection capability of ZnTe electro-optic field detectors, Appl. Phys. Lett.,* **68**, 2924-2926 (1996).

17. Zhang, X.-C., Hu, B.B., Darrow, J.T., Auston, D.H. *Generation of femtosecond electromagnetic pulses from semiconductor surfaces, Appl. Phys. Lett.*, **56**, 1011-1013 (1990).

18. Beard, M.C., Turner, G.M., Schmuttenmaer, C.A. *Measuring intramolecular charge transfer via coherent generation of THz radiation, J. Phys. Chem. A*, **106**, 878-883 (2002).

19. Cook, D.J., Hochstrasser, R.M. *Intense terahertz pulses by four-wave rectification in air*, *Opt. Lett.,* **25**, 1210-1212 (2000).

20. Hamster, H., Sullivan, A., Gordon, S., White, W., Falcone, R.W. *Subpicosecond, electromagnetic pulse from intense laser-plasma interaction, Phys. Rev. Lett.*, **71**, 2725-2728 (1993).

21. Woolard D.L., Brown R., Pepper M., Kemp M., *Terahertz frequency sensing and imaging: a time of reckoning future applications?* Proceedings of the IEEE **93** 1722 (2005).

22. Chen J., Chen Y., Zhao H., Bastiaans G., Zhang X.-C *Absorption coefficients of selected explosives and related compounds in the range of 0.1-2.8 THz*, Optics Express **15**, 12060 (2007).

23. A. Rusina, M. Durach, K. A. Nelson, and M.I. Stockman, "Nanoconcentration of terahertz radiation in plasmonic waveguides", Opt. Expr. **16**, pp. 18576 (2008).

24. D. Grischkowsky, S. Keiding, M. van Exter and Ch. Fattinger, "Far-infrared time-domain spectroscopy with terahertz beams of dielectrics and semiconductors," *J Opt. Soc. Am. B*, vol. 7, pp. 2006-2015, 1990.

25. J. D. Joannopoulos, R. D. Meade, and J. N. Winn, *Photonic Crystals: Molding the Flow of Light*, Princeton U. Press, 1995.

26. K. Sakoda, *Optical Properties of Photonic Crystals*, Springer, 2001.

27. S. G. Johnson and J. D. Joannopoulos, *Photonic Crystals: The Road from Theory to Practice*, Springer, 2002.

28. J.A. Dobrowolski, "Antireflection coating: key optical components," *SPIE* vol. 5963, pp. 596303-1 - 596303-12, 2005.

29. U. B. Schallenberg, "Antireflection design concepts with equivalent layers," *Appl. Opt.*, vol. 45, pp. 1507-1514, 2006.

30. C. R. Englert, M. Birk, and H. Maurer, "Antireflection coated, wedged, single-crystal silicon aircraftwindow for the far-infrared," *IEEE Trans. Geoscience and Remote Sensing*, vol. 37, pp. 1997-2003, 1999.

31. A. J. Gatesman, J. Waldman, M. Ji, C. Musante, and S. Yngvesson, "An anti-reflection coating for silicon optics at terahertz frequencies," *IEEE Microwave Guided Wave Lett.*, vol. 10, pp. 264-266, 2000.

32. T. Prasad, V. L. Colvin, and D. M. Mittleman, "The effect of structural disorder on guided resonances in photonic crystal slabs studied with terahertz time-domain spectroscopy," *Opt. Express*, vol. 15, pp. 16954-16965, 2007.

33. I. Hosako, "Multilayer optical thin films for use at terahertz frequencies: method of fabrication," *App. Opt.*, vol. 44, pp. 3769-3773, 2005.

34. D. Poitras, and J.A. Dobrowolski, "Toward Perfect Antireflection Coatings. 2. Theory," *App. Opt.*, vol. 43, pp. 1286-1295, 2004.

35. Y. Huang, S. Chattopadhyay, Y. Jen, C. Peng, T. Liu, Y. Hsu, C. Pan, H. Lo, C. Hsu, Y. Chang, C. Lee, K. Chen, and L. Chen, "Improved broadband and quasi-omnidirectional anti-reflection properties with biomimetic silicon nanostructures," *Nature Nanotech.*, vol. 2, pp. 770-774, 2007.

36. C. Bruckner, B. Pradarutti, O. Stenzel, R. Steinkopf, S. Riehemann, G. Notni, and A. Tunnermann, " Broadband antireflective surface-relief structure for THz optics," *Opt. Express*, vol. 15, pp. 779-789, 2007.

37. S. Kuroo, K. Shiraishi, H. Sasho, H. Yoda, and K. Muro, "Triangular surface-relief grating for reduction of reflection from silicon surface in the 0.1–3 terahertz region," *in 2008 Proc. CLEO*, pp. CThD7-1 - CThD7-2.

38. A. Thoman, A. Kern, H. Helm, and M. Walther, "Nanostructured gold films as broadband terahertz antireflection coatings," *Phys. Rev. B*, vol. 77, pp. 195405-1 - 195405-9, 2008.

39. C. Bruckner, T. Kasebier, B. Pradarutti, S. Riehemann, G. Notni, E. Kley, and A. Tunnermann, "Broadband Antireflective Structures for the THz Spectral Range Fabricated on High Resistive Float Zone Silicon," *in Proc. 2008 IRMMW-THz*, pp. F2K4.1485-1 - F2K4.1485-2.

40. E. Bassous, "Fabrication of novel three-dimensional microstructures by the anisotropic etching of (100) and (110) silicon," *IEEE Trans. Electron Devices*, vol. ED-25, pp. 1178-1185, 1978.

41. D. Resnik, D. Vrtacnik, R. Alkancic, M. Mozek and S. Almon, "The role of Triton surfactant in anisotropic etching of {110} reflective planes on (100) silicon," *J. Micromech. Microeng.*, vol. 15, pp. 1174-1183, 2005.

42. S. Rytov, "Electromagnetic properties of a finely stratified medium", *Soviet Phsyics JEPT*, vol. 2, pp. 466-475, 1956.

43. L. Escoubas, J.J. Simon, M. Loli, G. Berginc, F. Flory and H. Giovanni, "An antireflective silicon grating working in the resonance domain for the near infrared spectral region," *Opt. Commun.*, vol. 226, pp. 81-88, 2003.

44. B.E.A. Saleh and M.C. Teich, *Fundamentals of Photonics*, 2nd Ed., Wiley, 2007.

45. C. Bruckner, T. Kasebier, B. Pradarutti, S. Riehemann, G. Notni, E-B Kley and A. Tunnermann, "Broadband reflective structures applied to high resistive float zone silicon in the THz spectral range," *Opt. Exp.*, vol. 17, pp. 3063-3077, 2009.

46. P. Y. Han and X.-C. Zhang, "Time-domain spectroscopy targets the far-infrared", *Laser Focus World*, vol. 36, no. 10, pp. 117-121, 2000.

47. N. Karpowicz, J.M. Dai, X. Lu, Y.Q. Chen, M. Yamaguchi, H. Zhao, X.-C. Zhang, L. Zhang, C. Zhang, M. Price-Gallagher and C. Fletcher, "Coherent heterodyne time-domain spectrometry covering the entire terahertz gap", *Appl. Phys. Lett.*, vol. 92, pp. 011131-1 - 011131-3, 2008.

48. Y. W. Chen, P. Y. Han and X.-C. Zhang, "Tunable broadband antireflection structures for silicon at terahertz frequency," *Appl. Phys. Lett.*, vol. 94, pp. 041106-1 – 041106-3, 2009.

49. Mcknight, S.W.; Stewart, K.P.; Drew, H.D.; Moorjani, K. *Infrared Phys.* **1987**, *27*, 327–333.

50. Kroll, J.; Darmo, J.; Unterrainer, K. *Opt. Exp.* **2007**, *15*, 6552–6560.

51. Thoman, A.; Kern, A.; Helm, H.; Walther, M. *Phys. Rev. B.* **2008**, *77*, 195405-1 – 195405-9.

52. Chen, M.; Chang, H.; Chang, A.S.P.; Lin, S.; Xi, J.-Q.; Schubert, E.F. *Appl. Opt.* **2007**, *46*, 6533-6538.

53. Kadlec, C.; Kadlec, F.; Kuzel, P.; Blary, K.; Mounaix, P. *Opt. Lett.* **2008**, *33*, 2275-2277.

54. Ho, I.-C.; X. Guo, X.; Zhang, X.-C. Opt. Express. **2010**, *18*, 2872-2883.